NANYANG TECHNOLOGICAL UNIVERSITY

GLASS FRIT HERMETIC ENCAPSULATION FOR HARSH ENVIRONMENT MULTI-CHIP MODULE APPLICATION

Lim Jun Zhang

School of Materials Science & Engineering

Lim J.Z | Master Thesis | M.Eng (2013)

GLASS FRIT HERMETIC ENCAPSULATION

FOR HARSH ENVIRONMENT

MULTI-CHIP MODULE APPLICATION

LIM JUN ZHANG

School of Materials Science & Engineering

A thesis submitted to the Nanyang Technological University
in partial fulfilment of the requirement for the degree of
Master of Engineering

2013

ACKNOWLEDGEMENTS

Firstly, this author would like to express his gratitude to his school, School of Materials Science and Engineering. The school has equipped him with the necessary knowledge and skills in order for him to complete this project.

This author would also like to extend his sincere appreciation towards his supervisors, Assoc. Prof. Wong Chee Cheong and Assoc. Prof. Gan Chee Lip for giving him the opportunity to work under them for this project. He is also thankful to his supervisors for giving him suggestions and ideas to improve on this project.

He would also like to thank Eric Phua Jian Rong, Dr. I Made Riko, Dr. Ahmed Sharif, Lau Fu Long and Lim Ju Dy for assisting him in some of the experiments. In addition, he would also like to thank Dr. Vivek Chidambaram and Ho Beng Yeung from Institute of Microelectronics (IME) for the equipment support.

Last but not least, he would like to thank the laboratory technicians for providing equipment training and supply resources when in need.

Table of Contents

PAGE

ACKNOWLEDGEMENTS ii
LIST OF FIGURES vi
LIST OF TABLES viii
ABSTRACT ix
CHAPTER 1: INTRODUCTION 1
1.1 Background 1
1.2 Objectives 2
1.3 Scope 2
1.4 Organisation of report 3
CHAPTER 2: LITERATURE REVIEW 4
2.1 Hermeticity 4
2.1.1 Permeability of materials 4
2.1.2 Hermeticity testing 5
2.2 Bonding techniques comparison 6
2.2.1 Fusion bonding 6
2.2.2 Anodic bonding 7
2.2.3 Eutectic bonding 7
2.2.4 Thermo-compression bonding 8
2.2.5 Polymer gluing 8
2.2.6 Glass frit bonding 8
2.3 Glass frit bonding 9
2.3.1 Materials in glass frit paste 9
2.3.2 Processes of glass frit bonding 10
CHAPTER 3: EXPERIMENTAL TECHNIQUES 13
3.1 Sample preparation 13
3.1.1 Preparation of samples for shear tests 13
3.1.2 Preparation of samples for hermeticity tests 14
3.2 Sample characterisation 15
3.2.1 Differential scanning calorimetry 16
3.2.2 X-Ray inspection system 16
3.2.3 Scanning electron microscopy & energy dispersive spectroscopy 17

3.2.4 X-Ray diffraction 17

3.2.5 Shear tester 17

3.2.6 Vickers hardness tester 18

3.2.7 Nanoindentation 18

3.2.8 Three point bend tester 20

3.2.9 Helium leak detector & bomb chamber 22

3.2.10 Thermalgravimetric analysis 24

CHAPTER 4: RESULTS & DISCUSSION 25

4.1 Characterisation of AGC glass frit 25

4.1.1 DSC characterisation of AGC glass frit 25

4.1.2 XRD characterization of AGC glass frit 26

4.1.3 EDS performed on glass frit 27

4.1.4 TGA characterization of AGC glass frit 28

4.1.5 Fracture toughness of AGC glass frit 29

4.1.6 Flexural strength of AGC glass frit 32

4.1.7 X-Ray inspection on Al_2O_3 to Al_2O_3 bonding using glass frit 33

4.2 Shear strength of glass frit bonding under thermal aging 34

4.2.1 SEM image of thermal aged samples 34

4.2.2 Room temperature shear and hot temperature shear of thermal aged samples 36

4.2.3 SEM image of the surface of shear fractured samples 41

4.3 Helium leak test of glass frit bonded ceramic package under thermal aging 43

4.3.1 X-Ray inspection on ceramic package using glass frit bonding 43

4.3.2 Helium leak rate of ceramic package under thermal aging 44

4.3.2.1 Helium leak rate result of glass frit paste apply on encapsulation lid 44

4.3.2.2 Helium leak rate result of glass frit paste apply on both encapsulation lid and substrate 45

4.3.3 Difference in glass frit applied on single side and double side 46

4.3.3.1 SEM image of glass frit applied on single side and double side 46

4.3.3.2 Shear strength of glass frit applied on single side and double side 47

CHAPTER 5: SIMULATION 49

5.1 ANSYS™ simulation of package encapsulated with glass frit 49

5.1.1 Effect of hydrostatic pressure on the package 50

5.1.2 Effect of hydrostatic pressure on package with different glass frit thickness 53

5.1.3 Effect of hydrostatic pressure on package with a thicker encapsualtion lid 57

CHAPTER 6: CONCLUSION 59

CHAPTER 7: FUTURE WORK 61

REFERENCES 63

APPENDIX 1 68

LIST OF FIGURES

FIGURE **PAGE**

Figure 1.1: Hermetic encapsulated MCM 2

Figure 2.1: Permeability rates of sealing materials 5

Figure 2.2: Anodic bonding set up 7

Figure 2.3: Screen printing process 11

Figure 2.4: Voids formed in glass frit caused by insufficient heat treatment 12

Figure 2.5: Comparison of bonding with and without the use of barrier trench technology 12

Figure 3.1: Shear test samples 14

Figure 3.2: Suggested firing profile for AGC's glass frit paste (4115DS-1Ha) 14

Figure 3.3: Custom made metal stencil 15

Figure 3.4: Firing profile for sealing of package 16

Figure 3.5: Shear test perform on sample 18

Figure 3.6: Load-Displacement curve from Nanoindentation 19

Figure 3.7: Three point bend test setup 20

Figure 3.8: Cross sectional view of the sample 21

Figure 3.9: (a) Helium mass spectrometer and (b) Bomb chamber 23

Figure 4.1: Graph of DSC curve of glass frit 25

Figure 4.2: Graph of XRD pattern for glass frit heated to 290°C and 430°C 26

Figure 4.3: SEM image of glass frit at (a) 1500× and (b) 5000× magnification 28

Figure 4.4: TGA of AGC glass frit 29

Figure 4.5: Glass frit on glass slide that is screen printed and glazed for 15 times 30

Figure 4.6: Glass frit cracked on a piece of stainless steel after three point bend test 32

Figure 4.7: X-Ray inspection image of sample (a) with voids and (b) without void 34

Figure 4.8: SEM image of samples aged from 0 – 500 hours at 300°C 35

Figure 4.9: Room temperature and hot temperature shear strength of samples under thermal aging at 300°C for 1000 hours 36

Figure 4.10: SEM image of sample aged for 1000 hours at 300°C 40

Figure 4.11: Effect of temperature on the crack propagation in sodalime glass (from Wiederhorn and Bolz 1970) 40

Figure 4.12: SEM backscattered image of the fracture surface after shear test 42

Figure 4.13: X-Ray mapping of shear fractured surafce: (a) SEM image (b) Aluminium (c) Oxygen (d) Bismuth 42
Figure 4.14: A diagram showing the mixed mode of fracture of the shear test 42
Figure 4.15: X-Ray inspection image of a package sealed using glass frit bonding 43
Figure 4.16: Schematic diagram of (a) Single side (b) Double side 46
Figure 4.17: SEM image of (a) Single side (b) Double side 46
Figure 4.18: Shear test result for glass frit applied on single side and double side 47
Figure 5.1: Lid attached to base package design 50
Figure 5.2: Stress distribution of the encapsulation lid subjected to 207 MPa of hydrostatic pressure 51
Figure 5.3: Stress distribution of the base subjected to 207 MPa of hydrostatic pressure in: (a) Top down view (b) Bottom up view 52
Figure 5.4: Stress distribution of the glass frit subjected to 207 MPa of hydrostatic pressure 52
Figure 5.5: Directional deformation at z axis of the package subjected to 207 MPa of hydrostatic pressure 52
Figure 5.6: Stress distribution of the encapsulation lid with glass frit thickness of 0.00615 mm 53
Figure 5.7: Maximum principle stress at the centre region of encapsulation lid versus the glass frit thickness 54
Figure 5.8: Stress distribution of the glass frit with thickness of 10 mm 55
Figure 5.9: Stress distribution of glass frit with thickness of: (a) 0.00615 mm (b) 0.1 mm (c) 0.5 mm 56
Figure 5.10: Stress distribution of 6 mm thick encapsulation lid subjected to 207 MPa of hydrostatic pressure 57
Figure 5.11: Stress distribution of base with 6 mm thick encapsulation lid subjected to 207 MPa of hydrostatic pressure in: (a) Top down view (b) Bottom up view 58
Figure 5.12: Stress distribution of glass frit with 6 mm thick encapsulation lid subjected to 207 MPa of hydrostatic pressure 58
Figure 7.1: Shear test for ceramic-copper-glass frit-ceramic sample 62

LIST OF TABLES

TABLE **PAGE**

Table 2.1: Comparison between the bonding techniques 6

Table 3.1: Fixed conditions for test condition A_1 24

Table 4.1: EDS result of point 1 and 2 in Figure 4.3(b) 28

Table 4.2: Hardness readings from each Vickers indentation 31

Table 4.3: Fracture toughness readings 32

Table 4.4: Flexural load to flexural strength 33

Table 4.5: Glass frit thickness of samples 35

Table 4.6: Helium leak rate of package under thermal aging at 300°C for 500 hours (glass frit paste apply only on encapsulation lid) 44

Table 4.7: Helium leak rate of package under thermal aging at 300°C for 500 hours (glass frit paste apply on both encapsulation lid and substrate) 45

Table 5.1: Mechanical properties of AGC glass frit 49

ABSTRACT

This research project aims to investigate the suitability of glass frit bonding for multi-chip module (MCM) package encapsulation that needs to operate at a high temperature of 300°C and high pressure of 207 MPa. Since glass has the potential to bond well to alumina due to the chemical compatibility between the two materials, the use of glass frit for alumina to alumina bonding is considered a simple yet robust method that is often used for hermetic sealing of microelectronic packages. The materials used in the study were alumina substrate and bismuth-based glass frit paste 4115DS-1Ha from Asahi Glass Company (AGC). The study includes an initial characterisation of the glass frit, evaluation of the shear strength of the bonding, hermeticity test of the glass frit bonded MCM package and simulation on the high pressure testing on the package with glass frit. The average shear strength (shear test performed at 250°C) for samples after thermal aging at 300°C for 500 hours was 28.72 MPa. This value is approximately 3.6 times above the minimally required shear strength of 7.9 MPa according to the MIL-STD-883G specification. The hermeticity data of the sealed package after thermal aging at 300°C for 500 hours showed that the helium leak rate remained below the MIL-STD-883G specification of 5×10^{-8} atm cm^3/s. This proves that glass frit bonding for MCM hermetic encapsulation for high temperature application is feasible. ANSYS™ simulation was carried out and results showed that cracks would not form on the glass frit layer upon pressurising the package at 207 MPa since the maximum principle stress is below the flexural strength of the AGC glass frit.

CHAPTER 1: INTRODUCTION

1.1 Background

Industries that are dealing with extreme environment will have reliability issues with regards to the survivability of their electronic systems as their systems will be exposed to high temperature, pressure, radiation and corrosive environment. These types of industries include deep sea oil rigs, industrial chemical or nuclear plants, geological surveys, space vehicles, and military installations. In order to resolve these reliability issues, research work is proposed based on a multi-chip module (MCM) capable of sustaining hermeticity and withstanding the extreme conditions in the harsh environment.

It was reported that high temperature electronics for the exploration and monitoring of down-hole activities in geothermal wells and other oil and gas industry applications must reliably operate at a minimum temperature of 300°C for as long as 500 hours continuously [1]. Both leak rate and shear tests are methods used to evaluate the performance of the bonding layers and also to compare between different bonding techniques [2]. In terms of hermeticity, according to the MIL-STD-883G method 1014.9 standard, the leak rate rejection limit is 5×10^{-8} atm cm^3/s, therefore any package with leak rate above the rejection limit will be deemed to have failed [3].

Apart from being able to withstand the harsh environment, the design of the MCM ceramic package (refer to Figure 1.1) will require the encapsulation material to maintain hermeticity and be non-conductive as the signal lines will be running through the encapsulation seal. Furthermore, the sealing material has to be both planarising and chemically compatible to the surface of the ceramic lid and substrate.

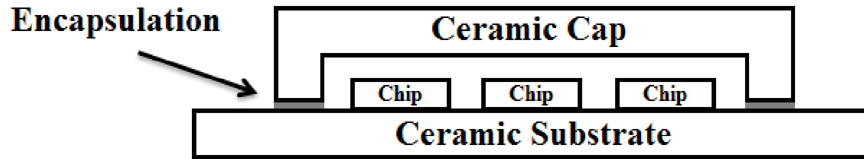

Figure 1.1: Hermetic encapsulated MCM

The use of glass frit bonding in wafer level encapsulation and packaging is common in microelectromechanical system (MEMS) [2-9], but it has yet to be explored for its use on alumina (Al_2O_3) MCM for high temperature and high pressure applications. In this proposed research, we will be investigating the practicality of using glass frit bonding for MCM hermetic encapsulation capable of withstanding the extreme conditions in the harsh environments with focus on glass frit bond.

1.2 Objectives

The objective of this project is to evaluate the use of glass frit bonding for Al_2O_3 MCM hermetic encapsulation at 300°C and high-pressure applications of 207 MPa for 500 hours.

1.3 Scope

The scope of this report encompasses primarily:

(a) Characterization of the glass frit

(b) The shear strength of ceramic to ceramic bonding under thermal aging at 300°C for 500 hours

(c) Hermeticity check on glass frit bonded Al_2O_3 MCM encapsulation under high temperature aging at 300°C for 500 hours

(d) ANSYS™ simulation on glass frit bonded Al_2O_3 MCM encapsulation

1.4 Organisation of report

The introduction presents an overview of glass frit bonding and the objectives of this study. The literature survey provides reader with the background knowledge needed to understand the method used and the results obtained from other researchers' work. The chapter on experiment techniques provides the reader with the methods used in the course of the research. The results and discussion section reports and analyses the results obtained from the research. These are rounded up with a conclusion which provides a summary of the report, highlighting the significance of the results obtained. The report ends with a recommendation of suggestions for improvements which can be made to the study as well as proposed ideas for future related studies.

CHAPTER 2: LITERATURE SURVEY

2.1 Hermeticity

Hermetic seal is the term used to describe a seal that is airtight and impervious to air or gas, moisture, humidity, and any external contaminants. High temperature electronics used in the exploration and monitoring of down-hole activities in geothermal wells and other oil and gas industry applications must have the ability to withstand high temperature of 300°C, high pressure of 207 MPa [10-11] and exposure to corrosive environments with hydrochloric acid (HCl) and hydrogen sulphide (H_2S) [4-5]. These two chemicals are extremely harmful to the circuitries and contacts with them must be avoided. In order to ensure the performance and sufficient reliability of the caped electrical components, hermetic sealing is required for this type of application [6-7].

2.1.1 Permeability of materials

The permeability rate of a material is the rate at which gas atoms are able to diffuse through the sealing material. The permeability rates can be compared between different types of materials of equal thickness and under standardised atmospheres [8]. The function of permeability is a combination of mass (g), distance (cm), time (s), and pressure (torr). Standard engineering practice would graph the permeability function as g/cm-s-Torr. Figure 2.1 shows different types of sealing materials with their permeability rate plotted. In the real physical world, there is no such thing as absolute or complete hermeticity because all materials are gas permeable to some degree. It shows that sealing materials like fluorocarbon, epoxies and silicones achieve less than 1 day of sealing capacity (10^{-14} g/cm-s-Torr) and are considered non-hermetic [9]. The materials considered hermetic are glasses and metals as sealing material of the same thickness of 10 μm has a lifetime of about a few years and 100 years respectively.

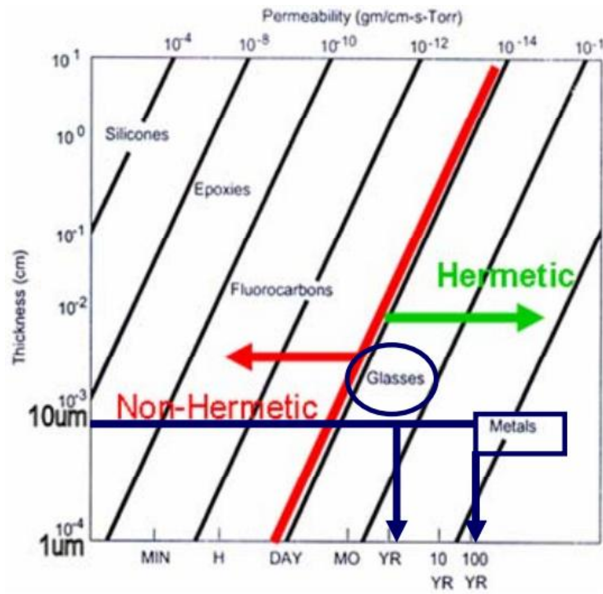

Figure 2.1: Permeability rates of sealing materials [9]

Jackson, K.A. et al. [12] reported that the free volume model for diffusion process in glass is when an atom jumps into an adjacent atom-size hole in the structure. This model assumes that the distribution of holes in the structure is a Boltzmann distribution whereby the probability of finding a space in the structure is extremely small [13]. Therefore, the diffusion rate for glass is low, making it ideal for hermetic encapsulation.

2.1.2 Hermeticity testing

Hermeticity test determines the robustness of the package and it is usually characterised by measuring the leak rate before and after the reliability test [14]. In terms of hermeticity test, sensitive methodologies and measurement tools are needed to detect the suspected leakages in small cavities [15] therefore fine leak test is done. A fine leak testing requires the package to be pressurized in a 100% helium atmosphere, also called the bomb chamber. This type of process is referred to as bombing. The sample is then placed in the helium leak detector to measure the leak rate of the helium from the cavity [16,17]. For encapsulated packages, according to the MIL-STD-883G specification, the maximum leak rate allowable is 5 x 10^{-8} atm cm^3/s [3].

2.2 Bonding techniques comparison

There is an extensive list of hermetic sealing techniques used in research and it includes glass frit bonding, thermocompression bonding, eutectic bonding, adhesive bonding, direct bonding and anodic bonding. Different bonding techniques have their own limitations and advantages [18]. Table 2.1 below shows a comparison between the bonding techniques:

Table 2.1: Comparison between the bonding techniques [19]

Method	Bonding Temperature (°C)	Topography Tolerance	Conductivity	Hermeticity
Fusion Bonding	1100	Very bad	Insulating	Good
Anodic Bonding	400	Bad	Insulating	Good
Eutectic Bonding (Au-Ge)	360	Good	Conducting	Good
Thermo-compression	340	Average	Conducting	Good
Polymer Gluing	100	Good	Insulating	Bad
Glass Frit Bonding	430	Good	Insulating	Good

2.2.1 Fusion bonding

Fusion bonding, also called direct bonding, requires two pieces of silicon substrate to be in close contact by applying a high contact force. Due to Van Der Waals forces, the substrates are held together and are strong enough for handling. The substrates are then annealed at high temperature to form a solid bond between them [8]. The drawback of fusion bonding is that the substrate surface quality has to be about 1-2 nm root mean square [20]. It is difficult for ceramics to achieve this kind of surface finish. Muller, B. et al. [21] has reported that silicon fusion bonding has a bond tensile strength of up to 20 MPa.

2.2.2 Anodic Bonding

Anodic bonding is widely used for bonding glass wafers as it is able to establish a hermetic and mechanically solid connection between glass and metal wafers or a connection between glass and semiconductor wafers [22-24]. Figure 2.2 shows the set up for anodic bonding. When electrostatic field is applied, the Sodium ions will be drifted away to cathode, leaving oxygen ions that are negatively charged to bond with the silicon at the glass and silicon interface. A downside of anodic bonding is that the residual gas generated during the bonding process might jeopardize the reliability of the device and sodium contamination [20,25-26]. Wei, J. et al. [22] reported that the bonding strength between glass and silicon wafers is higher than 10 MPa.

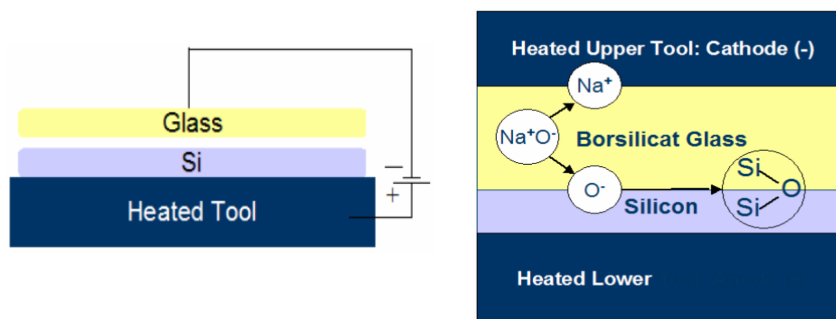

Figure 2.2: Anodic bonding set up [22]

2.2.3 Eutectic Bonding

Eutectic bonding involves bonding with mixture or alloy that has two or more dissimilar metals in the interlayer existing in eutectic system. The advantages of eutectic bonding are that metals have hundred times slower permeability than glass and it can provide electrical conductive paths in the device [27]. Jeong, B.G. et al. [28] report the use of fluxless Au-Sn solder system as the sealing material for the RF-MEMS packaging where the package was able to survive through a reliability test of 125°C for 1000 hours. On the other hand, Chidambaram, V. et al. [1] used Au-Ge solder system as a form of

interconnection and after thermal aged at 300°C for 500 hours, the shear strength performed at 250°C was 8 g/mil^2.

2.2.4 Thermo-compression bonding

Thermo-compression bonding requires two similar metals, e.g. copper or gold, to be in atomic contact by applying pressure and heat at the same time. Atomic contact allows diffusion reaction where atoms migrate from one crystal lattice location to another [29]. Tan, C.S. et al. [30] reported the use of copper-copper (Cu-Cu) thermo-compression bonding for MEMS and obtained a leak rate of 1.0-4.9 × 10^{-9} atm cm^3/s (lower than the MIL-STD-883G method 1014.9 standard limit). Additionally, Swinnen, B. et al. [31] reported that the Cu-Cu thermo-compression bonding on substrate, with the surface treated with dilute citric acid solution, has shear strength up to 90 MPa.

2.2.5 Polymer gluing

Polymer gluing can survive 20 years in clean environments at lower temperatures and the same can fail in a few days' time in corroding atmosphere at higher temperatures or pressures [5]. Despite the advantages of having low bonding temperature and being an inexpensive process [32], outgassing from polymers is a common problem as water and organic vapours are generated when the polymer cure [33]. Moisture ingress will reach the electronic components, and surface ions can allow electric shorting and degradation of the leakage-sensitive circuitry, promoting electronic failures [34].

2.2.6 Glass frit bonding

Glass frit bonding is an intermediate glass layer formed at the interface and is a technique that is universally useable for a wide range of application, normally for the packaging of MEMS [35-37]. The advantage of using glass frit bonding includes achieving hermetic

seal in moderately rough surfaces as the glass is able to wet the rough surface after it softens [6]. This is particularly suitable for ceramic substrate used for the MCM package as the surface finish requirements do not need to be tight. Glass also has the potential to adhere to ceramic components due to its chemical compatibility with ceramic [38]. In addition, it can even allow the signal lines to run through the sealing layer without affecting the hermeticity of the package [6,39-40]. This application advantage cannot be achieved in thermo-compression bonding and eutectic bonding as the bonding materials are conductive in nature. Furthermore, the suitability of glass frit bonding for industrial production is strongly attributed by the ease of sealant application, cost effective and high bonding yield of the process [19,41]. Chang, J.S. et al. [3] has reported a helium leak rate of about 10^{-9} atm cm^3/s (lesser than the MIL-STD-883G value) and an average shear strength of 34 MPa for MEMS packaging using glass frit bonding. Another research group Knechtel, R. et al. [39] has obtained a tensile strength of 20 MPa for using glass frit bonding on silicon. Moreover, Boettge, B. et al. [42] has reported that silicon to silicon bonded with glass frit bonding, after being thermal treated at 300°C for 48 hours, has pull test fracture strength of approximately 12 MPa.

2.3 Glass frit bonding

Glass frit bonding is the most suitable candidate of all the bonding techniques that can be considered for high temperature and high pressure application on MCM encapsulation due to the advantages stated above.

2.3.1 Materials in glass frit paste

Glass frit bonding requires the use of low melting point glass powder of approximately 400°C-450°C, organic binder, inorganic fillers and solvents [39]. The low melting glass powder is generally made up of network formers, modifiers and intermediates. Network

formers (e.g. SiO_2, B_2O_3, GeO_2 and P_2O_5) are oxide-forming glasses that can form 3D covalent networks via bridging oxygen. Network modifiers (e.g. Li_2O, K_2O, Na_2O, MgO, CaO and PbO) are ionic oxides added to lower the processing temperature by weakening the bonds and this decreases the glass transition temperature (T_g). For intermediates (e.g. Al_2O_3, TiO_2 and ZrO_2), they are additives that are added in small quantities to improve the thermal and mechanical behaviour of the glass by adding void space to the atomic structure and this allows room for flexure with the presence of voids [43]. There are two types of glass frits namely vitreous and devitrifying. Vitreous glass frit is thermoplastic in nature, melting and flowing each time when processed at sealing temperature. On the other hand, devitrifying glass frit is a thermosetting material that crystallises at the sealing temperature and its softening temperature increases upon crystallisation [8]. The organic binder transforms the glass powder into a printable viscous paste [6]. The inorganic fillers like cordierite particles (Mg_2Al_3 [$AlSi_5O_{18}$]) or barium silicate are used to lower the coefficients of thermal expansion (CTE) between the substrate and the glass frit material by adapting the CTE of the glass to the substrate materials to be bonded with [44]. In addition, it is able to improve the mechanical strength and resist cracks from propagating in the glass bond [7].

2.3.2 Processes of glass frit bonding

The bonding process involves screen printing, thermal conditioning and thermo-compressive [39]. The screen printing (refer to Figure 2.3) allows the paste to be deposited on a mesh opening depending on the particle size. With the help of a squeegee, the glass frit paste is printed on the substrate surface. The minimum line width of glass frit (depending on the screen printer) after printing is 150 μm but Chang, H.D. et al. [19] reported that with glass frit width of 50 μm, the helium leak rate is less than MIL-STD-883G method 1014.9 standard limit. It was also reported that the print yield increases

with the stencil opening of the screen printer and the yield approach to 95% when the print opening is larger than 75 μm [3].

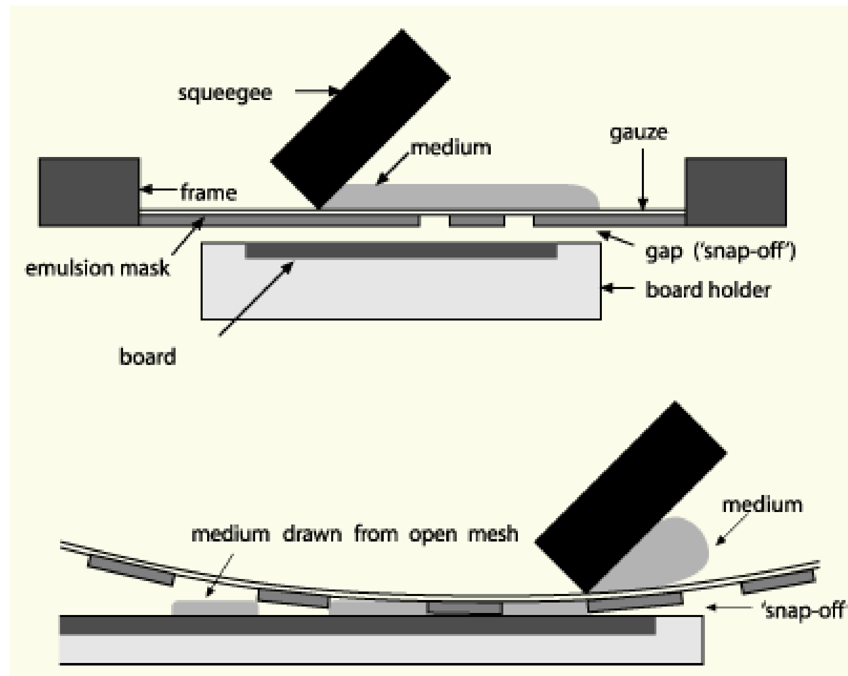

Figure 2.3: Screen printing process [45]

Upon thermo-conditioning, the binder, which consists of the organic additives and solvent, has already been burned out and the glass is pre-melted. This is the point where the paste is transformed into real glass. This step is very important as insufficient heat treatment can lead to the formation of voids inside the bonded glass (refer to Figure 2.4). The voids may lower the strength and reliability of the bonding due to lesser contact area [39].

The last step of the process is thermo-compressive bonding. The glass is heated to its wetting temperature at around 430°C and its viscosity decreases, wetting the surface of the substrate [20]. Being a thermal compressive bonding process, load is applied on the encapsulation lid to ensure that the lid has a close contact with the substrate surface [46]. The bonding pressure will depend on the design of the package and must be low enough to prevent any spreading of glass frit paste that can disturb the supposedly protected

device [6]. Chen, X. et al. [47] has reported that the solution to prevent the glass frit from reaching the device is to incorporate the barrier trench technology which is used on MEMS shown in Figure 2.5. It was reported that a load of 1000 mBar is applied throughout the heating and cooling process for MEMS packaging [19]. At this stage, the glass is melted and fused to the surface of the substrate at an atomic level and upon cooling a strong bond is formed [39]. The inorganic fillers are incorporated into the glass matrix without melting to lower the coefficients of thermal expansion (CTE) between the substrate and the glass frit material.

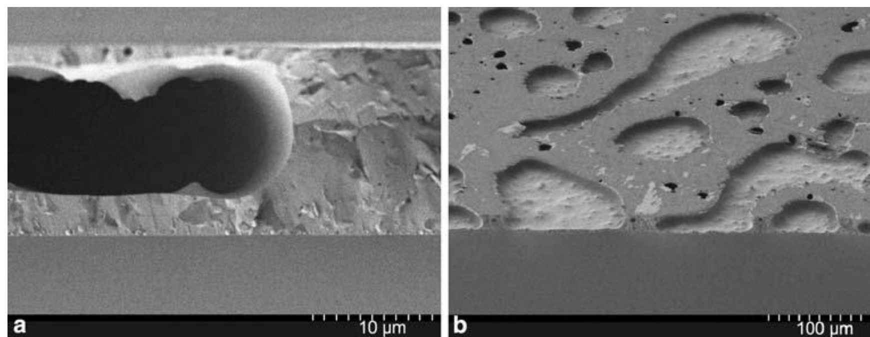

Figure 2.4: Voids formed in glass frit caused by insufficient heat treatment [39]

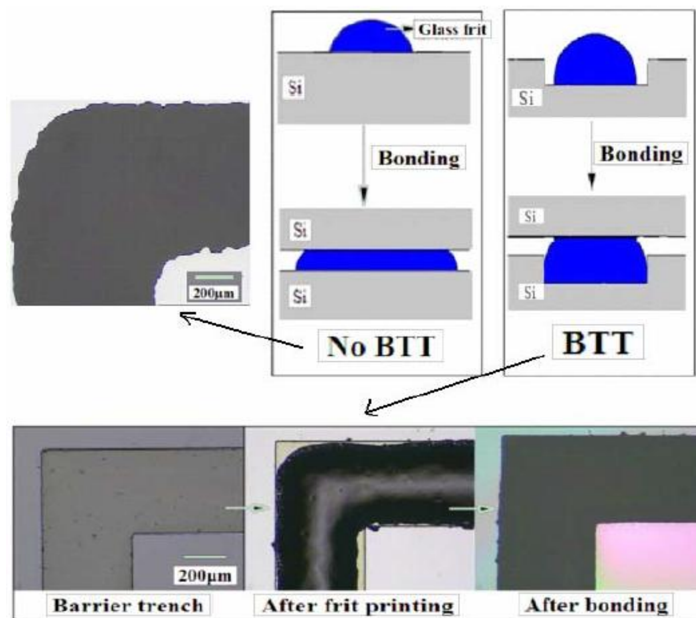

Figure 2.5: Comparison of bonding with and without the use of barrier trench technology [47]

CHAPTER 3: EXPERIMENTAL TECHNIQUES

3.1 Sample preparation

3.1.1 Preparation of samples for shear tests

The following elaborates on the procedure in the preparation of shear test samples:

1) Commercial Al_2O_3 substrate of thickness 0.76 mm was cut into 2.5 mm × 2.5 mm and 5 mm × 5 mm substrates.
2) The substrates were sent for ultrasonication with acetone for 5 minutes prior to usage.
3) Commercial Asahi Glass Company (AGC) glass frit paste (4115DS-1Ha) was applied onto the 2.5 mm × 2.5 mm substrates.
4) These 2.5 mm × 2.5 mm Al_2O_3 substrates were in turn joined to the 5 mm × 5 mm substrates shown in Figure 3.1.
5) The resulting samples substrates were then sent for heating in a calibrated Nabertherm box furnace using the suggested firing profile shown in Figure 3.2.
6) 0.15 MPa was applied on each sample during sealing.
7) After bonding, all the samples were sent for X-Ray inspection system to check for any presence of voids.
8) The samples were subsequently subjected to thermal aging of 100 hours, 300 hours and 500 hours at 300°C in the calibrated Nabertherm box furnace.
9) These samples were then sent for shear test using Dage series 4000 Shear tester at 25°C (Room temperature shear) and 250°C (Hot temperature shear).

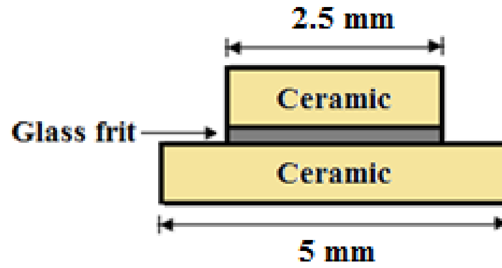

Figure 3.1: Shear test samples

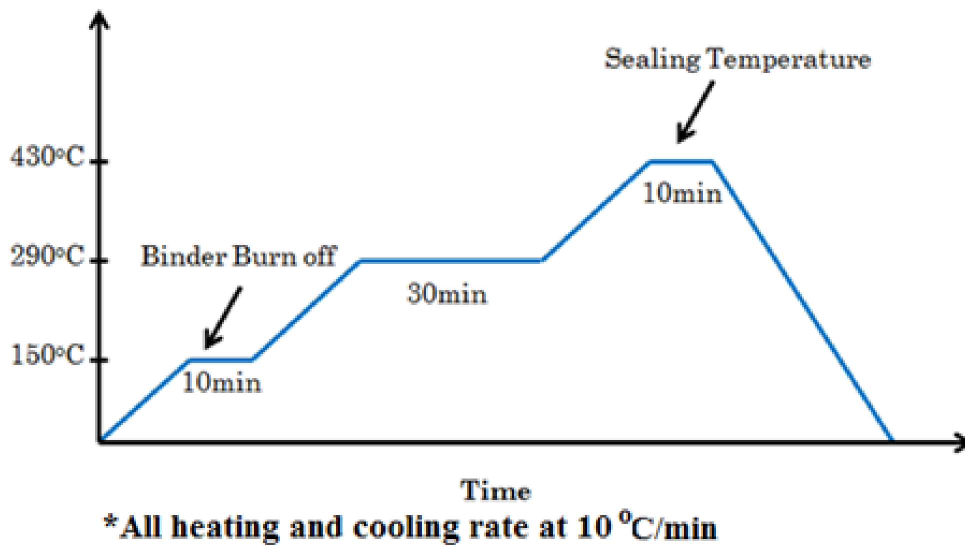

Figure 3.2: Suggested firing profile for AGC's glass frit paste (4115DS-1Ha)

3.1.2 Preparation of samples for hermeticity tests

The following elaborates on the procedure in the preparation of helium leak test samples:

1) Commercially bought Al_2O_3 encapsulation lid of dimensions 14 mm × 14 mm × 5 mm with a cavity of 10 mm × 10 mm × 3 mm and Al_2O_3 substrate of 15mm × 15 mm were sent for cleaning by ultrasonication with acetone for 10 minutes.
2) AGC glass frit paste was stencil printed, with the help of a custom made metal stencil and squeegee shown in Figure 3.3, on to the Al_2O_3 encapsulation lid and substrate.

3) The glass frit paste on the encapsulation lid and substrate was sent for thermo-conditioning (shown in Figure 3.4) to remove the solvent and organic binder.
4) After thermo-conditioning, the encapsulation lid was then joined to the substrate and sent for heating using the firing profile shown in Figure 3.4.
5) 0.15 MPa was applied on each sample during sealing.
6) After encapsulation, all the samples were sent for X-Ray inspection to check for any voids that are interconnected to each other.
7) The samples were subsequently subjected to thermal aging of 100 hours, 300 hours and 500 hours at 300°C in the calibrated box furnace.
8) These samples were then sent for helium leak test to obtain the helium leak rate.

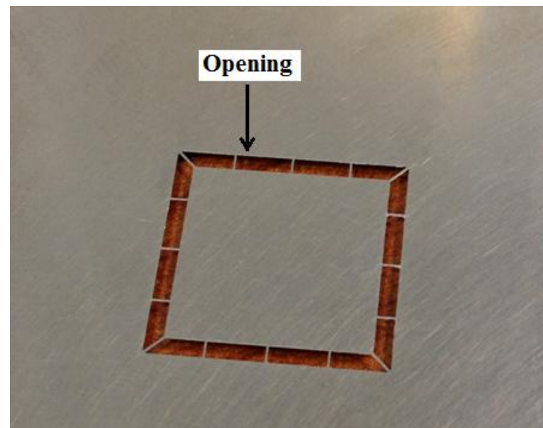

Figure 3.3: Custom made metal stencil

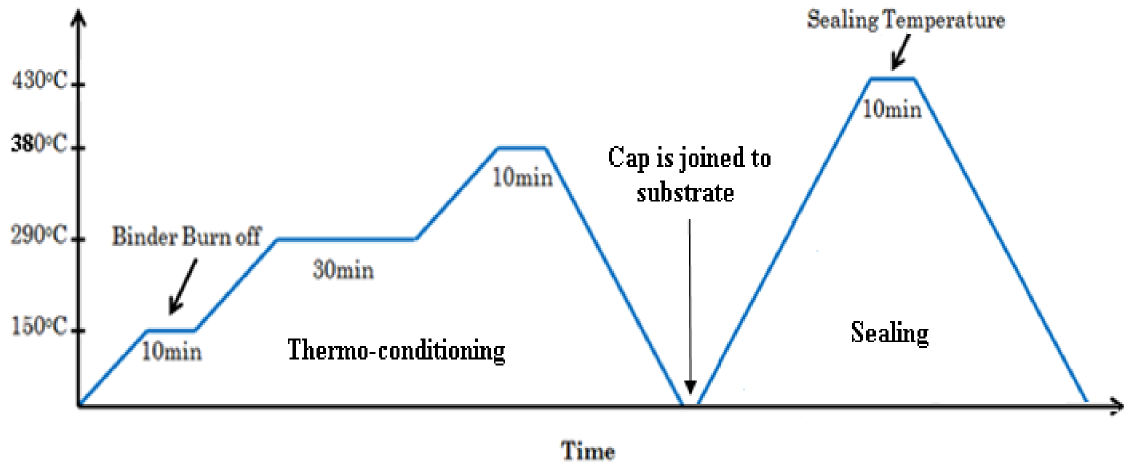

Figure 3.4: Firing profile for sealing of package

3.2 Sample characterisation

3.2.1 Differential scanning calorimetry

The Differential Scanning Calorimetry 404 Netzch (DSC) is a technique to measure the difference in the amount of heat required to increase the temperature of a sample against the reference as a function of temperature. The temperature of the sample and the reference are maintained the same. In order to maintain the same temperature, more or less heat will need to flow to the sample, which undergoes phase transitions, than the reference. DSC is used to determine the T_g of the glass frit. T_g is the reversible transition from a hard and relatively brittle state into a molten or rubber-like state and is a discontinuous change in the specific heat, energy, volume and viscosity of the material. The increase in specific heat will lead to an increase in the thermal lag of the sample relative to the reference, resulting in a shift in the baseline, or offset, of the curve.

3.2.2 X-Ray Inspection System

The Shimadzu SMX-2000EX X-Ray inspection system is a non-destructive testing (NDT) that uses X-Ray to penetrate the materials to give tomographical images. It is also used

for the inspection for any voids present in glass frit bonding as these voids form leakage path for moisture or corrosive gases to seep in and will no longer be hermetic [37].

3.2.3 Scanning electron microscopy & energy dispersive spectroscopy

The Scanning Electron Microscopy (SEM) (JEOL JSM-6360) and Energy Dispersive Spectroscopy (EDS) were used to determine visually the bonding quality and the composition of the glass frit that forms the bond between the ceramics respectively.

3.2.4 X-Ray diffraction

X-Ray diffraction (XRD) (Shimadzu 6000) was used to determine whether the glass frit is vitreous or devitrifying after the glass frit reaches the sealing temperature. If the sample is crystalline, it means that the glass frit is devitrifying and the identity of the sample is revealed by matching the measured intensities of the sample with the theoretical intensities at different 2theta angle using the Match! Software. The samples will be tested from the range of 10° to 80° at a rate of 2°/min. The fundamental law for XRD is Bragg's Law shown below:

$$n\lambda = 2d\sin\theta \quad -(1)$$

Where $\boldsymbol{n}$ is an integer,

$\boldsymbol{\lambda}$ is the wavelength of a beam of x-rays incident on a crystal

$\boldsymbol{d}$ is the distance of the separation of lattice planes, and

$\boldsymbol{\theta}$ is the Bragg angle.

3.2.5 Shear tester

The Dage series 4000 shear tester is to determine the shear strength (refer to Figure 3.5) of the glass frit bonding that has formed between the ceramics. This is based on a

measured force applied to the top ceramic substrate. According to the MIL-STD-883G specification, a minimum shear strength of 7.9 MPa is needed for the samples according to the glass frit area bonded between the ceramics [47].

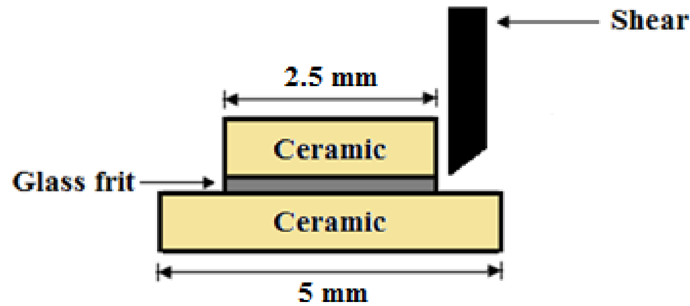

Figure 3.5: Shear test perform on sample

3.2.6 Vickers hardness tester

The Vickers hardness denotes a value obtained from a test load applied to a specimen to form an indentation on it with a square-based pyramidal diamond indenter which has face angle of 136°. The surface area of the permanent indentation found from its diagonal length was used to determine the hardness value using the following equation:

$$\mathrm{HV} = 0.1891\frac{\mathrm{F}}{\mathrm{d}^2} \quad -(1)$$

Where HV is the Vickers hardness,
F is the test load (N),
d is the Average diagonal length of an indentation (mm).

3.2.7 Nanoindentation

Nanoindentation is mainly used to evaluate materials hardness and elastic modulus at the submicron scale from the experimental recorded load-displacement data. The slope $\frac{dP}{dh}$ of the unloading curve (see Figure 3.6) is indicative of the stiffness of the contact.

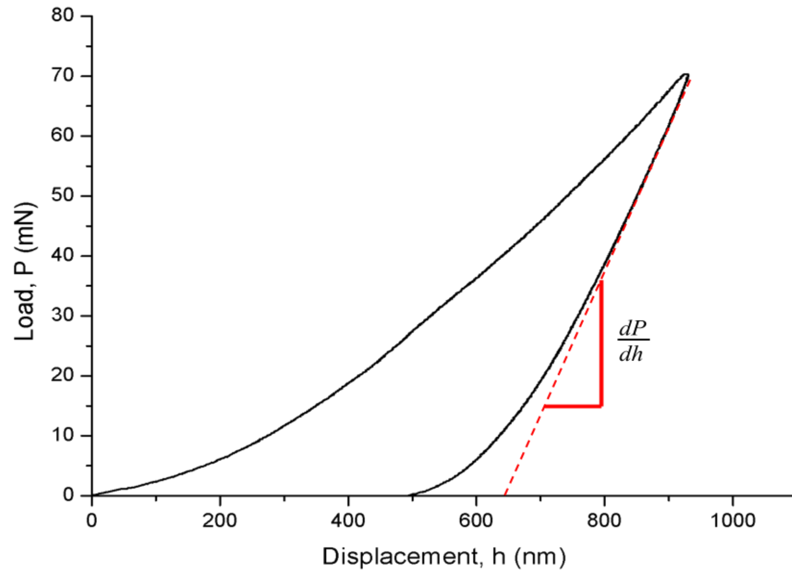

Figure 3.6: Load-Displacement curve from Nanoindentation

The reduced modulus of the material can be calculated using the following Eq. (1) [48]:

$$E_r = \frac{1}{2}\frac{\sqrt{\pi}}{\sqrt{A}}\frac{dP}{dh} \quad -(1)$$

Where E_r is the reduced modulus,

A is the area of contact,

P is the load,

h is the displacement.

To convert the reduced modulus to Young's modulus, the following Eq. (1) can be used:

$$\frac{1}{E_r} = \frac{(1-\upsilon^2)}{E} + \frac{(1-\upsilon_i{}^2)}{E_i} \quad -(1)$$

Where E is the Young's modulus,

E_i is the indenter's Young's modulus which is 1000 GPa [49],

υ_i is the Poisson's ration of the indenter which is 0.07 [49],

υ is the Poisson's ratio of glass frit (Assumption to be 0.3 [50]).

3.2.8 Three point bend tester

The purpose of using the three point bend tester (see Figure 3.7) is to determine the flexural strength, defined as the material's ability to resist deformation when under load, of the glass frit. The bending material will experience two types of stresses, namely the tensile stress (convex face) and compressive stress (concave face). The material usually fails under tensile stress rather than compressive stress. Therefore, the maximum tensile stress represents the flexural strength of the material before rupturing. In order to prepare the samples for the three point bend test, a layer of glass frit paste was applied on the surface of a piece of stainless steel plate (dimensions 115 mm × 24 mm × 1.46 mm) and sent for sintering to form a composite (see Figure 3.8). The flexural strength of the glass frit was determined upon its cracking in the composite.

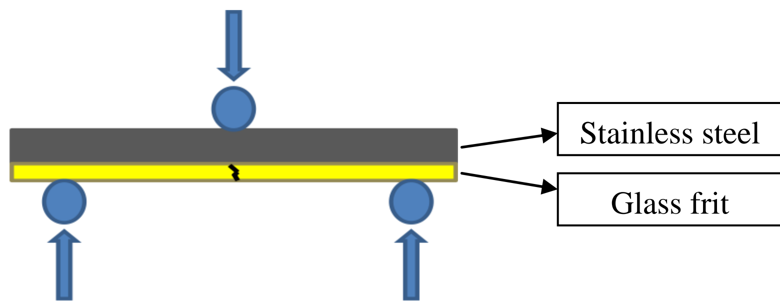

Figure 3.7: Three point bend test setup

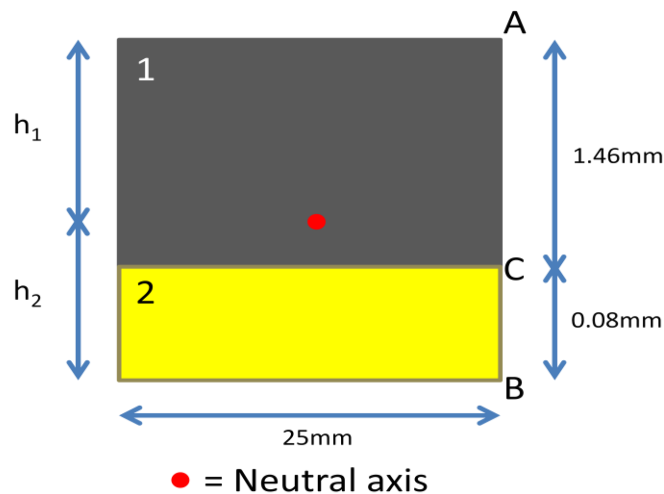

Figure 3.8: Cross sectional view of the sample

Firstly, the neutral axis of the composite (see Figure 3.8) has to be located in order to find h_1 and h_2 by using the following equations [51]:

$$E1\int_1 ydA + E2\int_2 ydA = 0 \quad -(1)$$

$$\int_1 ydA = \bar{y}1A1 \qquad \int_2 ydA = \bar{y}2A2 \quad -(2)$$

Where E is the Young's modulus,

$\bar{y}$ is the y coordinates of the centroids of the respective areas,

A is the area.

Secondly, the moment of inertia of A_1 and A_2 with respect to the neutral axis was determined by using the following equation:

$$I_x = I_{xc} + A\bar{y}^2 \quad -(1)$$

Where I_x is the moment of inertia with respect to the neutral axis,

I_{xc} is the moment of inertia,

$\bar{y}$ is the y coordinates of the centroids of the respective areas,

A is the area.

Thirdly, the bending moment acting at the midpoint of the specimen can be calculated using the following equation:

$$M = F \times D \quad -(1)$$

Where M is the bending moment,

F is the force needed to crack the material,

D is the distance and is half of the specimen.

Lastly, the flexural stress can be calculated using the flexure formula with the bending moment and moment of inertia being used in this formula:

$$\sigma_{2B} = -\frac{M(-h_2)E_2}{E_1 I_1 + E_2 I_2} \quad -(1)$$

Where σ_{2B} is the flexural stress that the glass frit experience on the surface B,
E_1 is the Young's modulus of the stainless steel (assuming to be 200GPa [52]),
E_2 is the Young's modulus of the glass frit (obtained using nanoindentation).

3.2.9 Helium leak detector and bomb chamber

The Varian helium mass spectrometer leak detector model 979 (see Figure 3.9(a)), which consists of turbomoleculer high vacuum pump and spectrometer tube, is used to detect the leak rate of the sealed package. The encapsulated package was pressurised in a sealed chamber (bomb chamber), as shown in Figure 3.9(b), with 95 - 100% of helium gas initially and transferred to the mass spectrometer immediately for leak rate detection.

The mathematical relationship of the above physical phenomenon can be represented by the following equation "Howell-Mann Equation" [8]:

$$R_m = \{(\beta R_{eq}\rho_e/\rho_o)\} \times \{1 - exp(\beta R_{eq} t_e/V\rho_o)\} \times \{exp(\beta R_{eq} t_d/V\rho_o)\} \quad -(1)$$

Where R_m is the measured leak rate of tracer gas helium through the leak
R_{eq} is the equivalent standard leak rate of air
M_a is the molecular weight of air,
M_h is the molecular weight of helium,
ρ_e is the bomb pressure of helium,

ρ_o is the atmospheric pressure,

t_e is the bomb time,

t_d is the dwell time, and

V is the volume of the cavity.

The equation $\beta = (M_a/M_h)^{\frac{1}{2}}$, which is the conversion relationship between different gases of interest, can be substituted into Eq. (1) above.

(a) (b)

Figure 3.9: (a) Helium mass spectrometer and (b) Bomb chamber

The first term of the equation $\{(\beta R_{eq}\rho_e/\rho_o)\}$ converts the true leak rate to that of helium. The second term $\{1 - exp(\beta R_{eq}t_e/V\rho_o)\}$ calculates the amount of helium entering the package during the bomb cycle t_e. The third term $\{exp(\beta R_{eq}t_d/V\rho_o)\}$ represents the amount of helium remaining in the package at test time t_d. Howell-Mann Equation assumes that all flow to be molecular and there is no helium sealed within the package.

According to the MIL-STD-883G specification, test method 1014.10 allows the use of the following table (Table 3.1) where the measured leak rate is related to the test parameter:

Table 3.1: Fixed conditions for test condition A_1

Volume of package (V) in cm^3	Bomb condition			R_1 Reject limit (atm cc/s He)
	Psia ±2	Minimum exposure time hours (t_1)	Maximum dwell hours (t_2)	
<0.05	75	2	1	5×10^{-8}
≥0.05 - <0.5	75	4	1	5×10^{-8}
≥0.5 - <1.0	45	2	1	1×10^{-7}
≥1.0 - <10.0	45	5	1	5×10^{-8}
≥10.0 - <20.0	45	10	1	5×10^{-8}

Based on the different volume of the internal cavities in the package, the bomb condition and rejection limit were used. The internal cavity volume of the ceramic package that was used for encapsulation is 0.3 cm^3. Thus, the sealed package was pressurised at 75 psia for 4 hours and the rejection limit of 5×10^{-8} atm cm^3/s helium according to the MIL-STD-883G specification was used.

3.2.10 Thermalgravimetric analysis

The Thermalgravimetric Analysis (TGA) was used to check for any decomposition in the glass frit when it was exposed to high temperature. It is a thermal analysis method that is used to measure any physical or chemical properties changes in the materials as a function of increasing temperature or time. Signs of decomposition can be observed when there is a drop in the weight of the sample.

CHAPTER 4: RESULTS & DISCUSSION

4.1 Characterisation of AGC glass frit

To find out and understand more about the AGC glass frit that is used for this proposed research, the following characterisation technique was done.

4.1.1 DSC characterisation of AGC glass frit

In order to ensure that the encapsulation material glass frit does not soften at temperature 300°C during usage, the T_g of the glass frit has to be determined. The graph below shows the DSC result of the glass frit paste that was heated to 1000°C at 5°C/min and cooled to room temperature at 5°C/min.

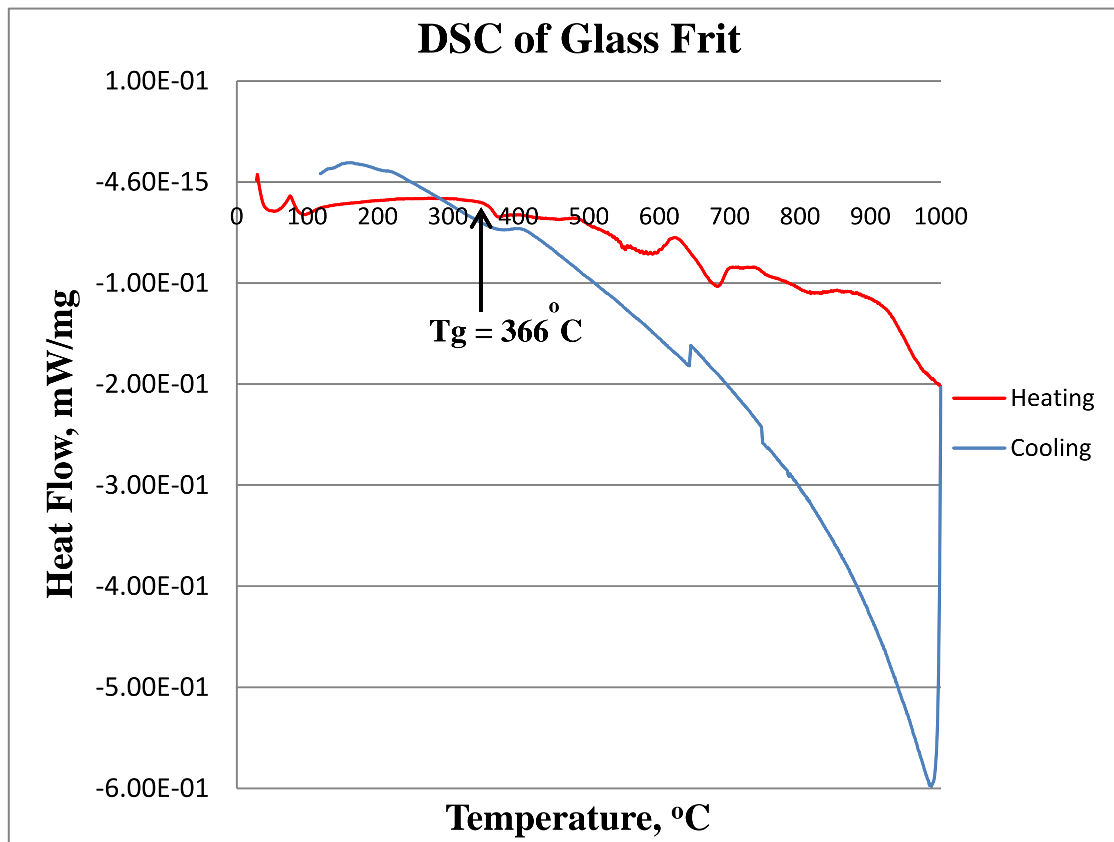

Figure 4.1: Graph of DSC curve of glass frit

It was stated previously that at the T_g point, the increase in specific heat will lead to an increase in the thermal lag of the sample relative to the reference and this results in a shift in the baseline, or offset, of the heating curve. On Figure 4.1, it clearly shows a shift in the baseline at about 366°C. The peak close to 100°C in heating curve resulted from the disturbance caused by the binder burnoff and diffusion of solvent out of the interface of the glass frit bonding. The peaks occurring between 500°C – 1000°C in the heating curve may be contributed by each of the oxides (network formers, modifiers and intermediates) present in the glass frit. There is no peak in the heating curve indicating the presence of melting temperature (see Figure 4.1). Similarly, there is no peak indicating the presence of crystallisation temperature in the cooling curve. Having T_g at 366°C prevents the glass frit from softening when the package is exposed to a temperature of 300°C.

4.1.2 XRD characterization of AGC glass frit

To determine whether the glass frit is vitreous or devitrifying after sealing temperature of 430°C, XRD was done for glass frit samples heated at 290°C and 430°C.

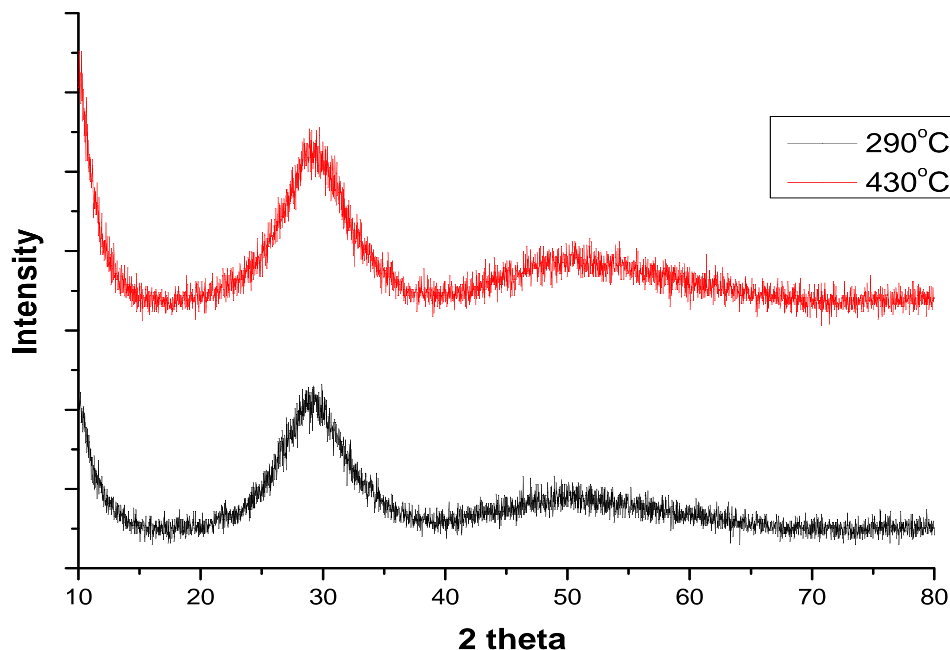

Figure 4.2: Graph of XRD pattern for glass frit heated to 290°C and 430°C

In Figure 4.2, the diffraction pattern graphics show that glass frits heated to 290°C and 430°C are amorphous in nature and present no long range order [53] unlike in crystallised structures, as seen from the broad XRD peaks of the graphs. This shows that the AGC glass frit is of vitreous type, where the material exhibits softening behaviour at sealing temperature. It allows users to carry out rework and reforming the poor seals if there is a need to replace any failed component in the capped package [54].

4.1.3 EDS performed on glass frit

To determine the composition in the AGC glass frit, EDS was performed. Figure 4.3(a) shows two pieces of ceramic substrates attached together with the glass frit as the intermediate layer. The EDS result of the glass frit in Figure 4.3(b) is shown in Table 1. Point 1 of Figure 4.3(b) is the matrix of the glass frit and the highest weight percentage is Bismuth, at 78.27 wt%. The bismuth-rich glass frit is an alternative for lead-based glass frit due to lead's potential harmful polluting effects to the environment [55]. Both Pb^{2+} and Bi^{3+} ions are highly polarisable, similar atomic weight and iso-electronic, therefore bismuth oxide is a suitable replacement for lead oxide in the lead-free glass frit [56-57]. Point 2 of Figure 4.3(b) is the inorganic fillers that are sealed to the glass matrix to minimise the thermal mismatch between the glass frit and the substrate [44]. The EDS result for point 2 contains 6.97 wt% of Magnesium.

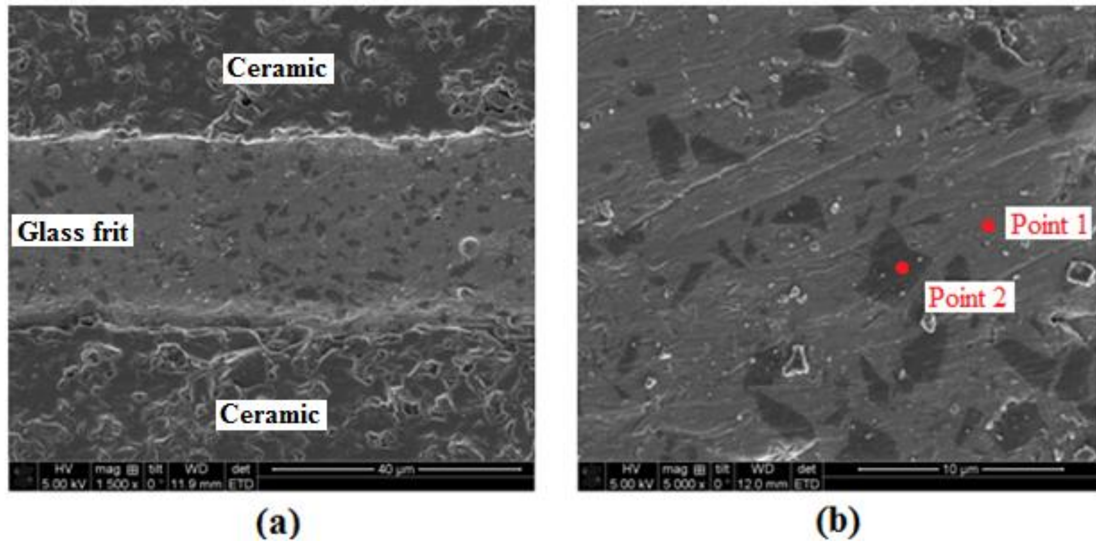

Figure 4.3: SEM image of glass frit at (a) 1500× and (b) 5000× magnification

Table 4.1: EDS result of point 1 and 2 in Figure 4.3(b)

Elements	**Point 1 wt%**	**Point 2 wt%**
Bismuth	78.27	41.43
Zinc	8.95	2.2
Aluminum	1.08	16.08
Silicon	0.76	23.34
Oxygen	10.93	9.98
Magnesium	-	6.97

4.1.4 TGA characterization of AGC glass frit

TGA is employed to check whether the glass frit decomposes at the thermal aged temperature of 300°C. The glass frit went through TGA for a few runs to check for possibility of decomposition of the glass frit. The results (see Figure 4.4) show that during the first run, the weight started to decrease from 43 mg to 40.4 mg at 100°C and when the temperature approaches 200°C, the weight remained constant. This indicates that at 100°C, due to the removal of organic binder and solvent, the weight decreased slightly.

Subsequent reruns show that the weight does not have significant changes and therefore the glass frit does not decompose even at a temperature of 1000°C.

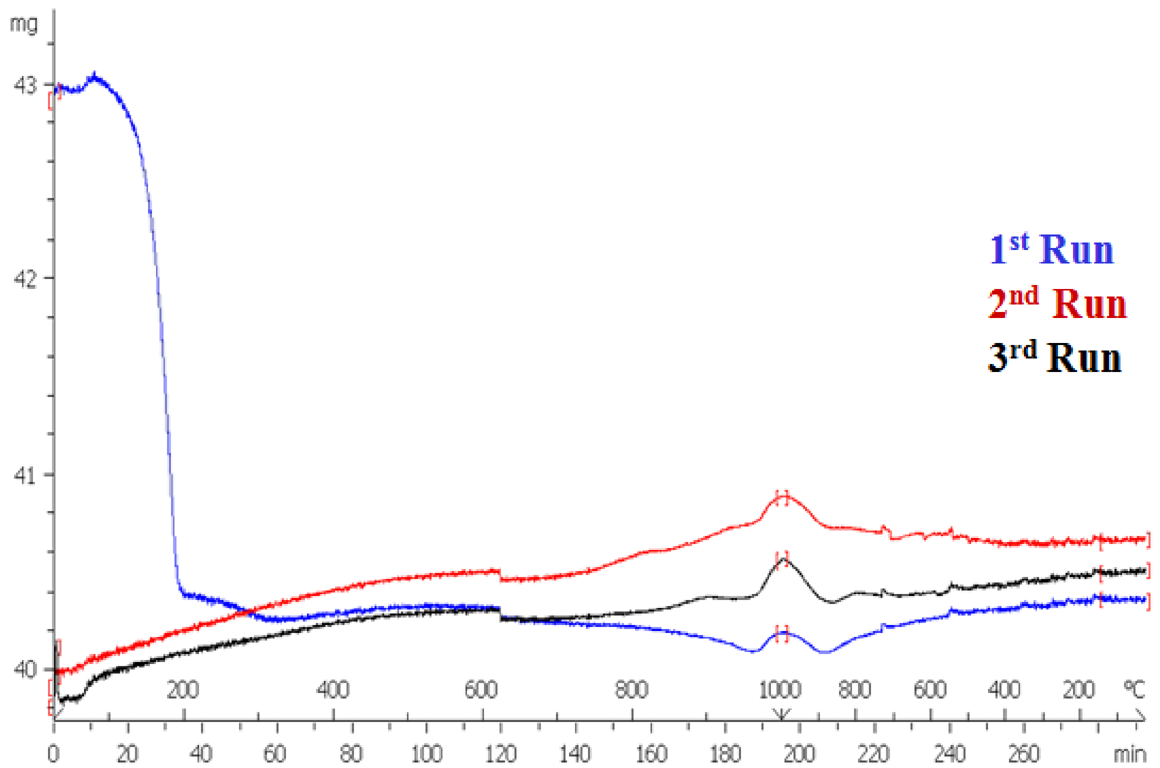

Figure 4.4: TGA of AGC glass frit

4.1.5 Fracture toughness of AGC glass frit

To find out the fracture toughness of the AGC glass frit, the Young's modulus and the hardness of the glass frit have to be obtained using Eq. (1) and (2) [58] below:

$$H = \frac{P}{a_o a^2} \quad -(1)$$

$$K_c = \xi_v^R (E/H)^{\frac{1}{2}} \left(P/c_o^{\frac{3}{2}}\right) \quad -(2)$$

Where K_c is the fracture toughness

P is the indentation peak load,

C_o is the crack length,

ξ_V^R is 0.016, which is a material-independent constant,

E is the Young's modulus (calculated from Nanoindenter),

H is the materials hardness (Vickers hardness test),

a is the half diagonal of the indentation length,

a_o is 2, which is a numerical constant for the Vickers indenter.

The sample thickness for both Nanoindenter and Vickers hardness tester requires a thick layer of glass frit. As such, the glass frit paste was screen printed on a piece of glass slide and sent for glazing numerous times. This process was repeated for 15 times on the same area (see Figure 4.5). The thickness of the glass frit on the glass slide has to be more than 850 µm as it is the limit that the surface profiler can measure.

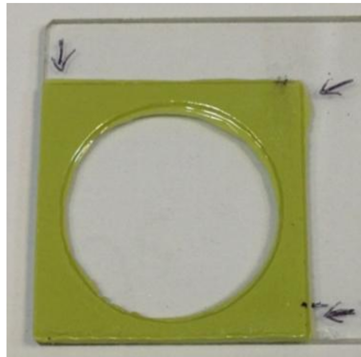

Figure 4.5: Glass frit on glass slide that is screen printed and glazed for 15 times

The reduced modulus value was derived from the nanoindentations and the tests were done using a Berkovich indenter with an apex semi-angle (θ = 65.27°) and effective cone angle (α = 70.3°). It is then converted to the Young's modulus readings from 40 indentations shown in Appendix 1 to derive an average value of 58.97 GPa with a standard deviation value of 3.175. This falls within the literature value of the Young's modulus of oxide glass, which ranges between 50 – 90 GPa [59].

The glass frit hardness value was derived from the Vickers hardness tester and 1 kgf of load was used for each indentation. The table below shows the values of the material's hardness from each indentation:

Table 4.2: Hardness readings from each Vickers indentation

Indentation	Hardness (GPa)
1	4.299
2	4.423
3	4.573
4	4.403
5	4.371
Average	**4.414**
Standard Deviation	**0.1**

The hardness of the glass frit was concluded to be approximately 4.414 GPa, falling within the literature range of 2 - 8 GPa [60] for oxide glasses. The bottom of the glass slide was inspected for any cracks penetrating through the glass frit for each indentation point so as to ensure the accuracies of the glass frit hardness value.

The average value of Young's modulus (E) and hardness (H) were 58.97 GPa and 4.414 GPa respectively. The applied force P is 9.807 N (1 kgf of load). Taking these constant values and the crack length C_o of each indentation in the Vickers hardness test, the fracture toughness K_c was calculated and recorded in the table below:

Table 4.3: Fracture toughness readings

Crack Length (µm)	Fracture Toughness (MPa√m)
51.8	1.538
56.1	1.364
53.6	1.460
46.9	1.788
44.5	1.934
Average	**1.617**
Standard Deviation	**0.237**

The average fracture toughness of the glass frit was calculated to be 1.617 MPa√m, as shown above.

4.1.6 Flexural strength of AGC glass frit

To determine the flexural strength of the glass frit, the three point bend test was used in this experiment where failure (presence of cracks) was ensured to occur only on the glass frit and not on the base material (see Figure 4.6).

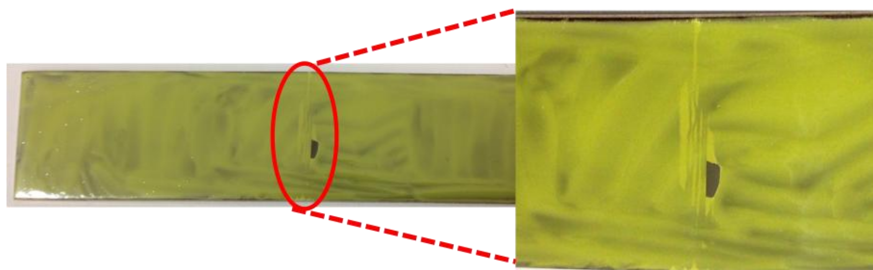

Figure 4.6: Glass frit cracked on a piece of stainless steel after three point bend test

The flexural load was measured when the glass frit cracks and with the help of the equations shown in Chapter 3.2.8, the flexural load and the calculated flexural strength are recorded in the following Table 4.4:

Table 4.4: Flexural load to flexural strength

Flexural Load (N)	Flexural Strength (MPa)
303.4	152.72
300.7	152.24
295.3	149.76
Average	152
Standard Deviation	1.589

The average flexural strength of the glass frit, as shown above, is 152 MPa. Both material properties, fracture toughness and flexural strength of the glass frit, are applied in ANSYS™ simulation (see Chapter 5) to investigate the ability of glass frit to withstand a high hydrostatic pressure of 207 MPa.

4.1.7 X-Ray inspection on Al_2O_3 to Al_2O_3 bonding using glass frit

Knechtel, R. et al. [39] reported that insufficient heat treatment could lead to the formation of voids inside the bonded glass. To inspect for voids formed after bonding, X-Ray inspection was performed on all the bonded samples. Figure 4.7(a) shows the sample without load applied during sealing process where large voids can be clearly seen in the bonded area using X-Ray inspection system. Figure 4.7(b) shows the sample with a pressure of 0.15 MPa applied during the sealing process and it was observed to be void-free. The glass frit bonding is similar to the thermo-compression technique as heat and pressure are applied at the same time. This technique allows the binder gas to be squeezed out of the glass frit and for glass frit to fuse with the Al_2O_3. Since all the bonded samples were determined to be free of voids, it clearly demonstrates that the suggested heating profile provides sufficient heat treatment to the glass bond.

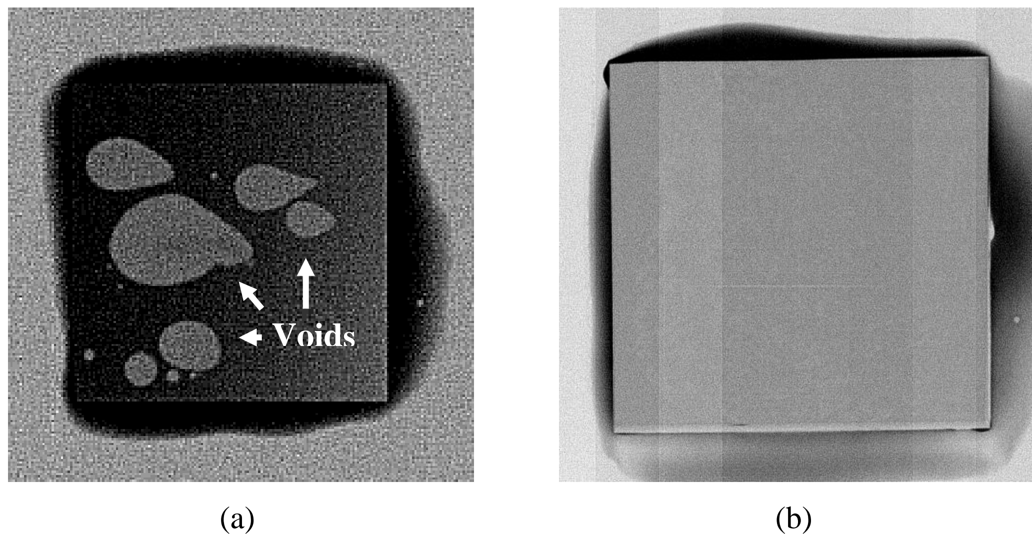

(a) (b)

Figure 4.7: X-Ray inspection image of sample (a) with voids and (b) without void

4.2 Shear strength of glass frit bonding under thermal aging

In order to determine the bonding strength of glass frit bonding under thermal aging, the Al_2O_3 samples, bonded using glass frit, were subjected to aging at 300°C for 500 hours. After thermal aging, the cross sectional details of one sample from each batch was viewed under SEM. The rest of the samples were sheared under the temperature of 25°C (Room temperature shear) and 250°C (Hot temperature shear) using the shear tester.

4.2.1 SEM image of thermal aged samples

To ensure that the thermal aged samples adhere well to each other through glass frit bonding, SEM image were taken for samples aged from 0 – 500 hours at 300°C.

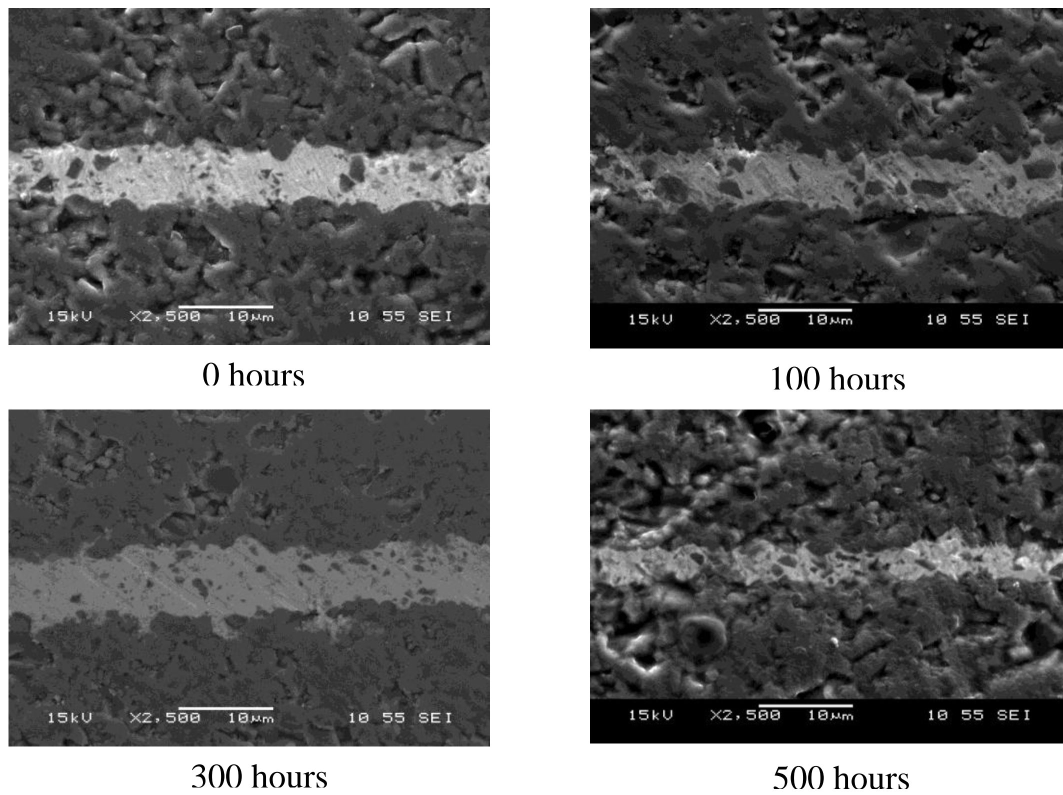

Figure 4.8: SEM image of samples aged from 0 – 500 hours at 300°C

Figure 4.8 clearly shows that all the samples adhered well to each other with glass frit bonding even after thermal aging for 500 hours at 300°C. The flowability of the glass frit is superior as it is able to flow to the undulating surface of the ceramic upon heating to T_g. The glass frit thicknesses for the sample are shown in Table 4.5.

Table 4.5: Glass frit thickness of samples

Sample	Glass frit thickness (μm)
0 hours	6.2
100 hours	6.4
300 hours	7.4
500 hours	4.6

In Table 4.5, it shows the glass frit thickness of the SEM images shown in Figure 4.8. The thicknesses of samples taken from each batch were found to fall within the sub-micron range (i.e. 4.6 - 7.4 μm). All the sheared sample surfaces showed that the mode of failure was a mix of cohesive and adhesive failure. If the glass frit thickness is much thicker, the fracture would likely not propagate from one interface to the other, thus resulting in cohesive failure generally. On the other hand, if the glass frit thickness falls below sub-micron range values, fracture will likely occur solely on the interface, resulting in adhesive failure.

4.2.2 Room temperature shear and hot temperature shear of thermal aged samples

For room temperature shear and hot temperature shear, the samples are sheared at 25°C and 250°C, respectively. The results are shown as follows:

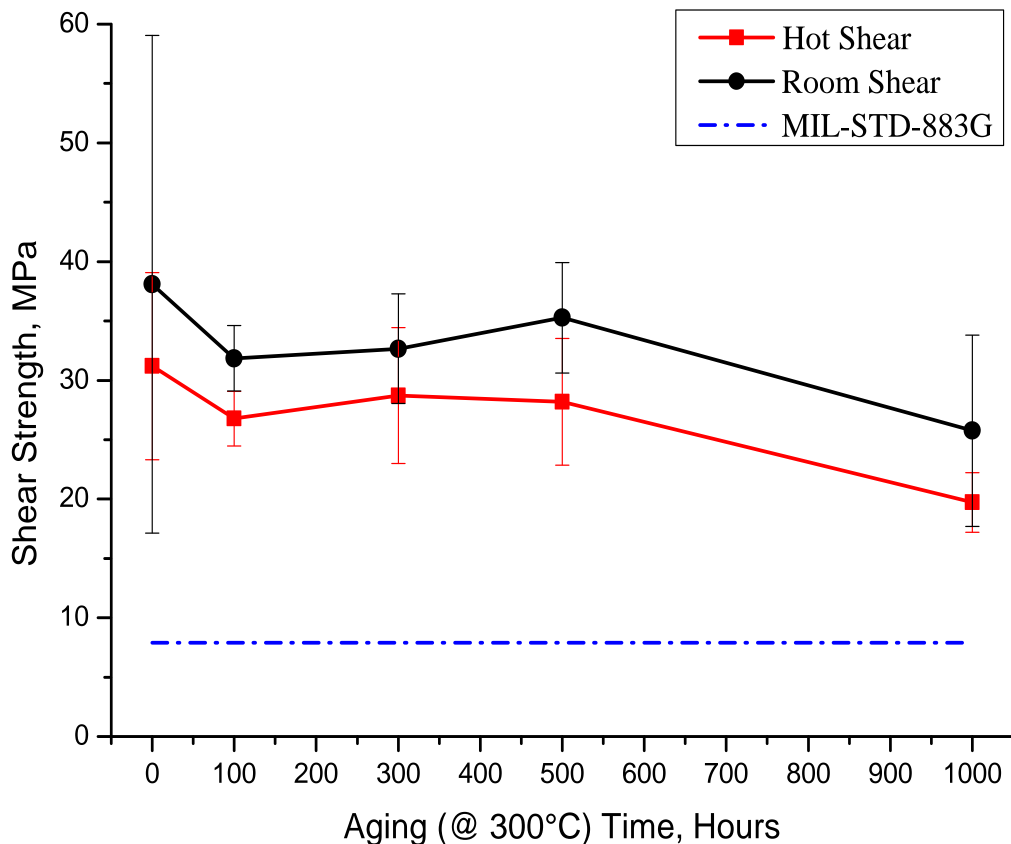

Figure 4.9: Room temperature and hot temperature shear strength of samples under thermal aged at 300°C for 1000 hours

Figure 4.9 shows that all the samples exhibit shear strength above the minimally required shear strength of 7.9 MPa according to the MIL-STD-883G specification before and after thermal aging. This could be because the T_g of the glass frit is 366°C and the aging (300°C) and hot temperature shear (250°C) temperature are both not high enough to cause significant weakening of bonds between the oxides or deterioration of the adhesion strength between the glass frit and ceramic. The room temperature shear was higher than hot temperature shear for samples thermal aged from 0 hours to 500 hours and this could be explained by a slight weakening of the adhesion strength between the glass frit and ceramic during hot temperature shear at 250°C. There was a slight drop in shear strength for room temperature shear and hot temperature shear from 0 hours to 100 hours aging. This may be caused by damages to the glass frit internal structure during the initial period of exposure to the aging temperature. According to Griffith, A.A., the theoretical strength of glass is always higher than the strength obtained from practical work due to the unavoidable presence of small flaws in the glass [61]. These small flaws are sub-micrometric cracks that are inconspicuous and escape notice under optical inspection [62]. Likewise, flaws also exist in glass frit bonding. When samples were thermal aged at 300°C, the prolonged thermal aging acts as a form of stress concentrator and accelerates the corrosive influence of the environment (primarily water vapour) on the glass [63]. This effect significantly sharpens the crack tip radius to a molecular dimension and promotes slow crack growth with the stress-corrosion reactions concentrating at the crack tip. This leads to a slight drop in shear strength after thermal aging at 300°C for 100 hours.

The induced thermal shock on samples when they were removed promptly from the furnace for cooling after thermal aging can also be a possible reason behind the sudden drop in shear strength after 100 hours of aging. Thermal stresses induced during rapid cooling of a glass introduce flaws. Heating glasses for a prolonged period has also been

shown to reduce their strength due to the formation of a small number of surface crystals, or the bonding of dust particles to the glass surface [60]. In either case, a thermal expansion mismatch creates local flaws during cooling. During thermal shock, stress is generated at the surface due to instantaneous cooling while the bulk is still at the original temperature. The amount of stress generated due to thermal shock can be calculated by using the following Eq. (1):

$$\sigma = \frac{E\alpha\Delta T}{(1-\upsilon)} \quad - (1)$$

Where σ is the stress due to thermal shock,

E is the Young's modulus (58.97 GPa, obtained from nanoindentation),

ΔT is the temperature difference between surface (25°C) and bulk (300°C),

α is the thermal expansion coefficient of glass frit, and

ν is the Poisson's ratio (Assumption to be 0.3 [50])

The maximum stress experienced by the glass frit caused by thermal shock is calculated to be 95.35 MPa. Although this is lower than the flexural strength of the glass frit, it may cause minute flaws in the glass frit that cause the drop in shear strength.

From 100 hours to 500 hours of aging, the average hot temperature shear strength of 28.72 MPa remained almost constant. A good shear strength was achievable because of the coefficient of thermal expansion (CTE) mismatch between the Al_2O_3 substrate (8.2×10^{-6} /°C) and glass frit (8.4×10^{-6} /°C) is very small. Eq. (1) below was used to calculate the shear stress imposed due to CTE mismatch:

$$\gamma = (\alpha_b - \alpha_c)(T_{max} - T_0) \quad - (1)$$

$$\gamma = (8.4 \times 10^{-6} - 8.2 \times 10^{-6})\ (300\text{-}25)$$

$$= 5.5 \times 10^{-5}$$

$$\sigma = G\gamma$$

$$\sigma = 26.2 \text{ x } 5.5 \times 10^{-5} = 0.001441 \text{ GPa}$$

Where γ is the Shear strain

α_b is the Thermal expansion coefficient of glass frit,

α_c is the Thermal expansion coefficient of Al_2O_3 substrate,

T_{max} is the Maximum temperature (300°C),

T_0 is the Room temperature (25°C),

σ is the Shear stress,

G is the Shear modulus of glass frit (assumed to be 26.2 GPa [64]).

The shear stress calculated is 1.441 MPa. Since this magnitude of stress is comparatively small, there was no sign of delamination for the samples.

In order to determine the limits of glass frit bonding, the samples were aged till 1000 hours. A 30% dropped of hot temperature shear strength to 19.72 MPa was observed. The SEM image in Figure 4.10 shows the interface of the sample aged for 1000 hours, where there seems to be good adherence with glass frit as the intermediate layer. Although the SEM image shows good adherence between the ceramics and the glass frit, there is still a drop in shear strength upon aging at 300°C for 1000 hours. This could be due to the stress corrosion effect. We understand that the low strength of glass is contributed by the unavoidable presence of small flaws in the glass and these small flaws are submicrometric cracks that often go unnoticed under optical inspection. With long duration of thermal aging as a form of stress concentrators, the corrosive influence of the environment on the glass is accelerated. This effect will significantly sharpen the crack tip and leads to weakening of the internal structure of the glass frit. Thus, although the SEM image shows good adherence between the alumina and the glass frit, in actual fact, the strength of the

glass has been lowered. The graph (see Figure 4.11) of the crack propagation velocity as a function of the applied stress intensity factor (stress state near the tip of the crack) derived in a study done by Wiederhorn and Bolz in 1970 [65] shows that as temperature increases, the graph will shift towards the left as the crack propagation velocity (υ) increases with temperature at a constant stress intensity factor (K_1).

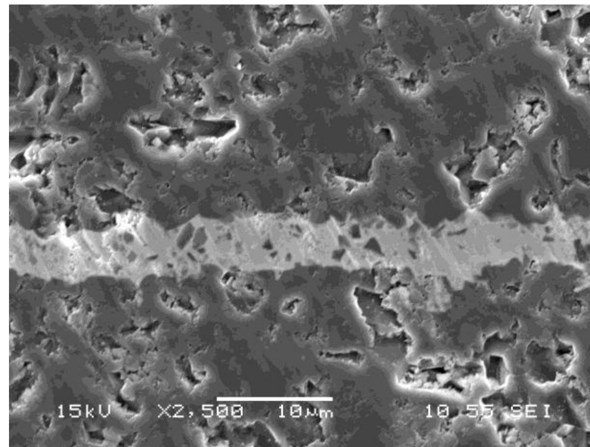

Figure 4.10: SEM image of sample aged for 1000 hours at 300°C

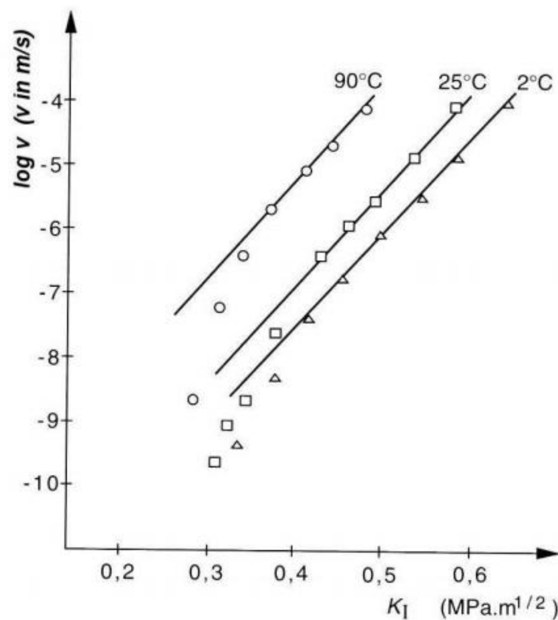

Figure 4.11: Effect of temperature on the crack propagation in sodalime glass (from Wiederhorn and Bolz 1970 [65])

Despite aging for 1000 hours, both the hot temperature shear and room temperature shear strength (see Figure 4.9) remained well above the required shear strength of 7.9 MPa, as stated under the MIL-STD-883G specification. This shows the potential of glass frit bonding in withstanding high temperature of 300°C even till 1000 hours.

4.2.3 SEM image of the surface of shear fractured samples

The surfaces of the shear fractured samples were inspected using the SEM (see Figure 4.12). In Figure 4.13 (a), the black regions consist of both aluminium (see Figure 4.13 (b)) and oxygen (see Figure 4.13 (c)) which implies the presence of Al_2O_3. Using X-Ray mapping, the white regions in Figure 4.13 (a) consists of bismuth (see Figure 4.13 (d)) and it implies the presence of the bismuth-based glass frit. Likewise in Figure 4.12, the black regions are Al_2O_3 and the white regions are bismuth-based glass frit. It was observed that there were traces of Al_2O_3 on the glass frit and also Al_2O_3 surface being exposed with no glass frit on both top and bottom of the samples. This shows that it is a mixed mode of fracture consisting of both cohesive and adhesive failure or simply to say it fails by alternate fracture shown in Figure 4.14. The normal glass cleavage morphology (mirror, mist and hackle morphology) does not apply to the glass frit under shearing. This is due to the alumina fillers and micro voids that are present in the glass frit. The fillers deflect the direction of the cracks propagate, creating a tortuous path for the cracks [39] and the shearing force direction from the side of the sample, thereby giving a different type of morphology.

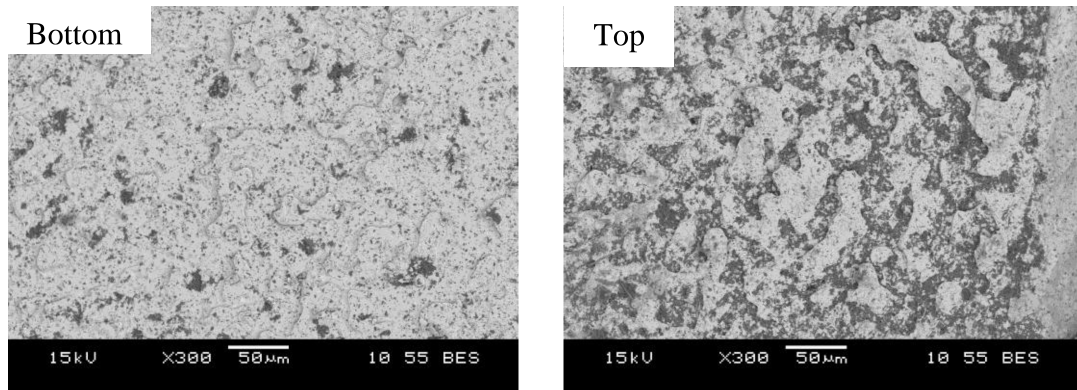

Figure 4.12: SEM backscattered image of the fracture surface after shear test

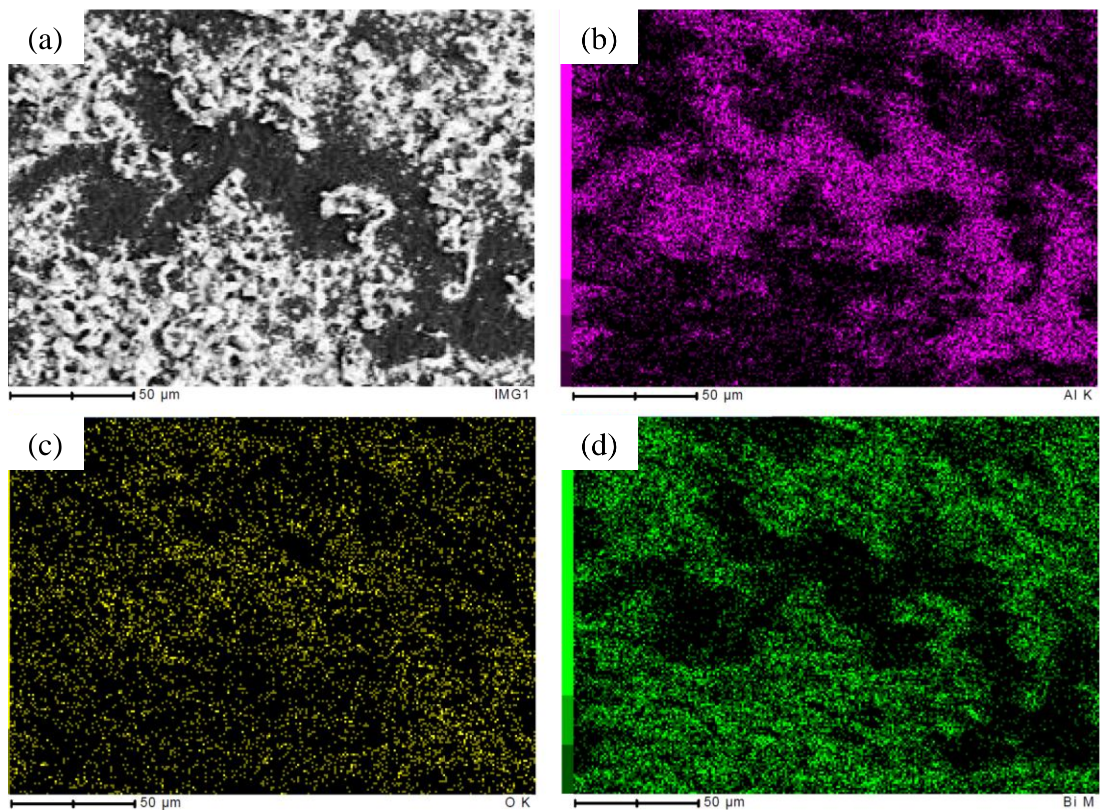

Figure 4.13: X-Ray mapping of shear fractured surface: (a) SEM image (b) Aluminium (c) Oxygen (d) Bismuth

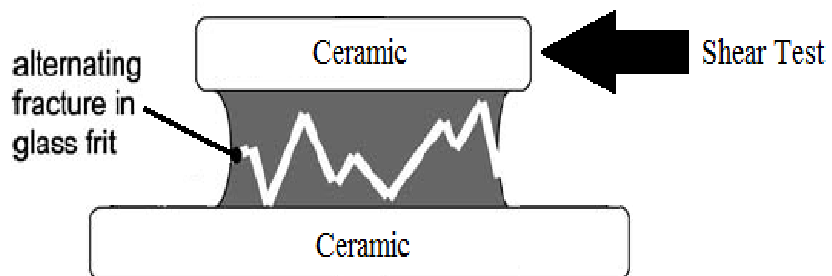

Figure 4.14: A diagram showing the mixed mode of fracture of the shear test

4.3 Helium leak test of glass frit bonded ceramic package under thermal aging

Despite having a good shear strength for ceramic to ceramic joining using glass frit as the intermediate layer even after exposing to high temperature of 300°C for 500 hours, helium leak test has to be done in order to determine whether prolonged thermal aging affects the hermeticity of the ceramic package.

4.3.1 X-Ray inspection on ceramic package using glass frit bonding

To inspect for the formation of voids after bonding, X-Ray inspection was performed on all the bonded packages. Figure 4.15 shows the package after sealing with glass frit bonding and voids were observed in the bonded area using X-Ray inspection system. The reason for voids to be present in the sealed area is that the sealed area has a larger area as compared to the experiment using 2.5 mm × 2.5 mm ceramic substrate to find out the shear strength of glass frit. The larger sealed area resulted in organic binders being trapped in the matrix of the glass frit. Despite the appearance of voids in the sealed area, the hermeticity of the package was not affected as the key to hermeticity is that there must be no interconnecting voids creating a leakage path from the internal package to the external environment.

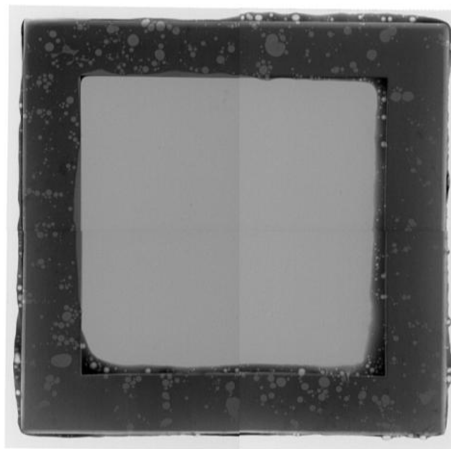

Figure 4.15: X-Ray inspection image of a package sealed using glass frit bonding

4.3.2 Helium leak rate of ceramic package under thermal aging

The helium leak test makes use of the helium detector to measure the leak rate of the sealed package that was previously pressurised with helium when placed in the bomb chamber. According to the MIL-STD-883G specification, the rejection limit to the 0.3 cm^3 cavity package will be 5×10^{-8} atm cm^3/s helium.

4.3.2.1 Helium leak rate result of glass frit paste apply on encapsulation lid

Table 4.6: Helium leak rate of package under thermal aging at 300°C for 500 hours (glass frit paste apply only on encapsulation lid)

Sample	0 hour	100 hours	300 hours	500 hours
	Leak rate (atm cm^3/s helium)			
S1	4.1×10^{-8}	5.8×10^{-8}	1.7×10^{-7}	6.3×10^{-8}
S2	1.1×10^{-8}	4.0×10^{-7}	1.1×10^{-7}	8.0×10^{-8}
S3	4.5×10^{-8}	4.1×10^{-8}	1.0×10^{-7}	3.9×10^{-8}
S4	3.2×10^{-8}	1.7×10^{-7}	5.3×10^{-8}	6.5×10^{-8}
S5	3.2×10^{-8}	6.8×10^{-8}	5.6×10^{-8}	5.1×10^{-8}

Table 4.6 shows the helium leak rate of the ceramic packages, where glass frit paste is only applied onto the encapsulation lid. The packages underwent thermal aging at 300°C for 500 hours. Although the samples survived before being subjected to thermal aging, all the helium leak rates of the samples fell above the rejection limit of 5×10^{-8} atm cm^3/s after 300 hours of thermal aging at 300°C.

According to the shear test results, glass frit bonding remained strong and the shear strength remained almost constant even after thermal aging at 300°C for 500 hours. This shows that the glass frit material and bonding with ceramic have the ability to withstand

this harsh temperature. The postulated reason for the failure of all the samples is the application of glass frit paste on only one surface of the package. Therefore, more tests were conducted with the application of glass frit paste on both the encapsulation lid and substrate before sealing together.

4.3.2.2 Helium leak rate result of glass frit paste apply on both encapsulation lid and substrate

Table 4.7: Helium leak rate of package under thermal aging at 300°C for 500 hours (glass frit paste apply on both encapsulation lid and substrate)

Sample	0 hour	100 hours	300 hours	500 hours
	Leak rate (atm cm^3/s helium)			
S6	1.5×10^{-8}	3.1×10^{-8}	1.4×10^{-8}	2.7×10^{-8}
S7	1.5×10^{-8}	2.0×10^{-8}	1.9×10^{-8}	1.6×10^{-8}
S8	2.3×10^{-8}	1.3×10^{-8}	1.4×10^{-8}	9.2×10^{-8}
S9	1.9×10^{-8}	2.6×10^{-8}	3.5×10^{-8}	3.8×10^{-8}
S10	5.9×10^{-9}	1.5×10^{-8}	1.7×10^{-8}	4.7×10^{-8}

Table 4.7 shows the helium leak rate of the ceramic packages, where glass frit paste is applied onto the encapsulation lid and substrate, underwent thermal aging at 300°C for 500 hours. The results show that all the samples were able to achieve hermeticity up to 300 hours and upon reaching 500 hours, all samples passed the helium leak test except for sample S8. This shows that glass frit bonding can be used for MCM hermetic encapsulation for high temperature application as four out of five samples passed the helium leak test. Sample S8 might have failed the test due to inherent inconsistency resulting from the manual application of glass frit.

4.3.3 Difference in glass frit applied on single side and double side

In order to determine the difference between glass frit applied on single side (see Figure 4.16(a)) and on double side (see Figure 4.16(b)), shear test was performed on the joints made by applying the glass frit on one side (Single side) and both sides (Double side) of the ceramics substrate before sending for thermo-conditioning.

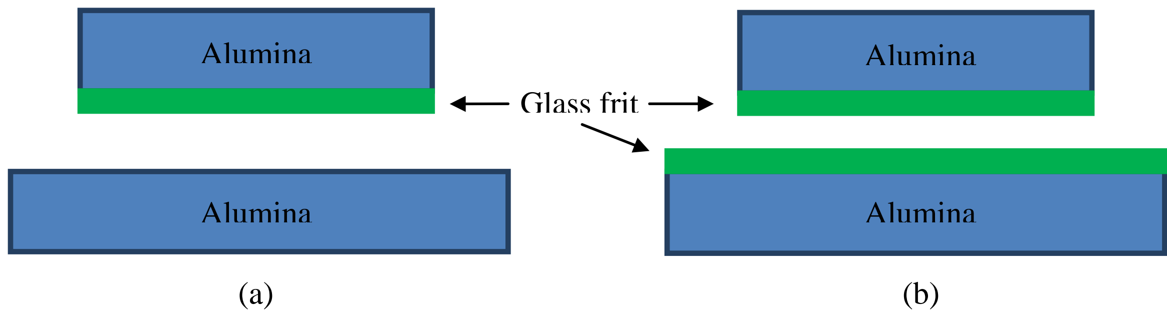

Figure 4.16: Schematic diagram of (a) Single side (b) Double side

4.3.3.1 SEM image of glass frit applied on single side and double side

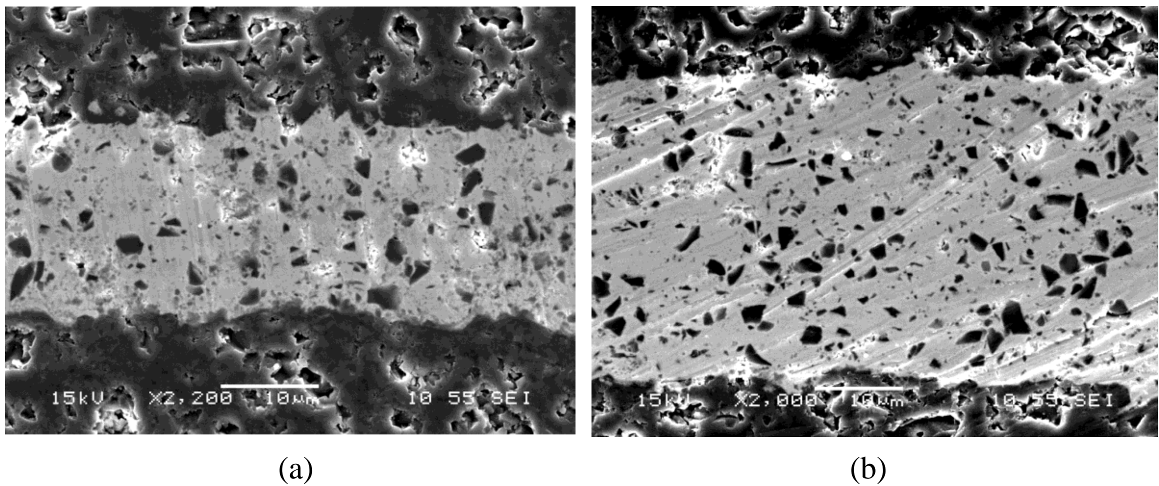

Figure 4.17: SEM image of (a) Single side (b) Double side

From the SEM image as seen in Figure 4.17, no difference was observed in the structure of the glass frit for both single and double side. Both the images show that the glass frit adhered well to the Al_2O_3 surface. The only difference is the thickness of the glass frit as

the single side has only one side applied with glass frit paste but for double side, has both encapsulation lid and substrate applied with glass frit paste.

4.3.3.2 Shear strength of glass frit applied on single side and double side

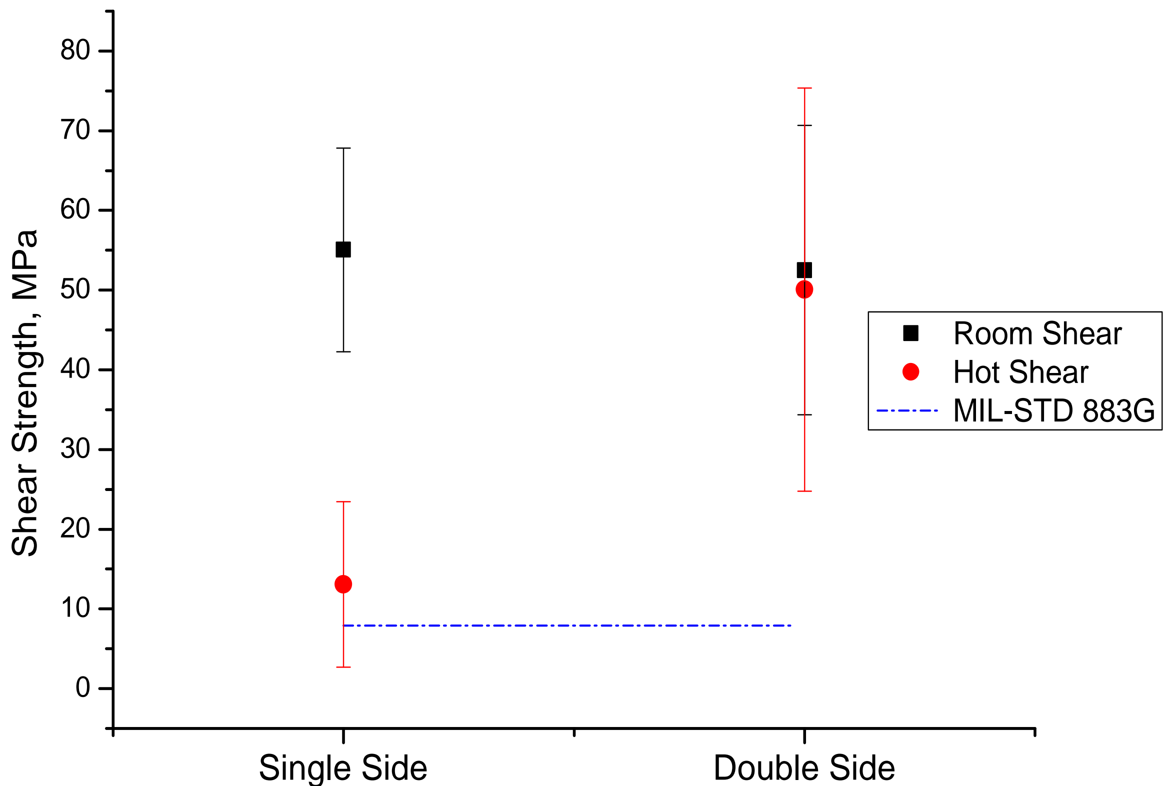

Figure 4.18: Shear test result for glass frit applied on single side and double side

For room temperature shear, as seen in Figure 4.18, whether glass frit was applied on single or double side, there is no effect on the shear strength as both the shear strength that are of approximately 50 MPa. However, the difference was evident after hot temperature shear performed at 250°C. The samples with single side applied with glass frit presented a prominent drop in the shear strength with some with shear strengths falling below the rejection limits. For samples with both sides applied with glass frit, there was only a slight drop in the average shear strength. Therefore, these may be the

reason for sample S1-S5 to fail the helium leak test after going through thermal aging at 300°C. For the case of the single side, only the encapsulation lid is applied with glass frit paste and goes through the thermo-conditioning step (see Figure 3.4), therefore the glass frit has more bonding strength to the surface of the encapsulation lid. Upon thermal aging, the interface between the glass frit and the substrate on single side gets weakens and delaminates easily. As for the double side, both the encapsulation lid and substrate have glass frit paste being applied on them before undergoing the thermo-conditioning step and during the sealing stage both side of glass frit on the double side soften and merged together to form a glass frit bond.

CHAPTER 5: SIMULATION

5.1 ANSYS™ simulation of package encapsulated with glass frit

To determine the possibility of using glass frit as a sealing material for encapsulated packages that can withstand high hydrostatic pressure of 207 MPa and whether the glass frit can withstand cooling from joining temperature, ANSYS™ simulation was performed. In Chapter 4, the mechanical properties of AGC glass frit were found and are tabulated as follow:

Table 5.1: Mechanical properties of AGC glass frit

Properties	Value
Fracture Toughness	1.617 MPa√m
Flexural Strength	151.906 MPa
Young's Modulus	58.97 GPa
Hardness	4.09 GPa

The mechanical properties of the AGC glass frit in Table 5.1 were used in the simulation to determine whether the sealing layer will crack under high hydrostatic pressure. The design of the package in this simulation is similar to the experiment conducted in the hermeticity test, whereby an Al_2O_3 encapsulation lid of dimensions 14 mm × 14 mm × 5 mm with a cavity of 10 mm × 10 mm × 3 mm was attached to the Al_2O_3 substrate base of 14 mm × 14 mm with a layer of glass frit of thickness 0.00615 mm (see Figure 5.1). The average glass frit thickness was derived from Table 4.5. In the simulation, the package was subjected to a hydrostatic pressure of 207 MPa. The bottom face of the package was selected to be the fixed support to prevent sliding from occurring when hydrostatic pressure was applied. Subsequently, the thickness of the glass frit was changed to 0.1 mm

and 0.5 mm to investigate the effect of different glass frit thicknesses on the stress distribution on the package.

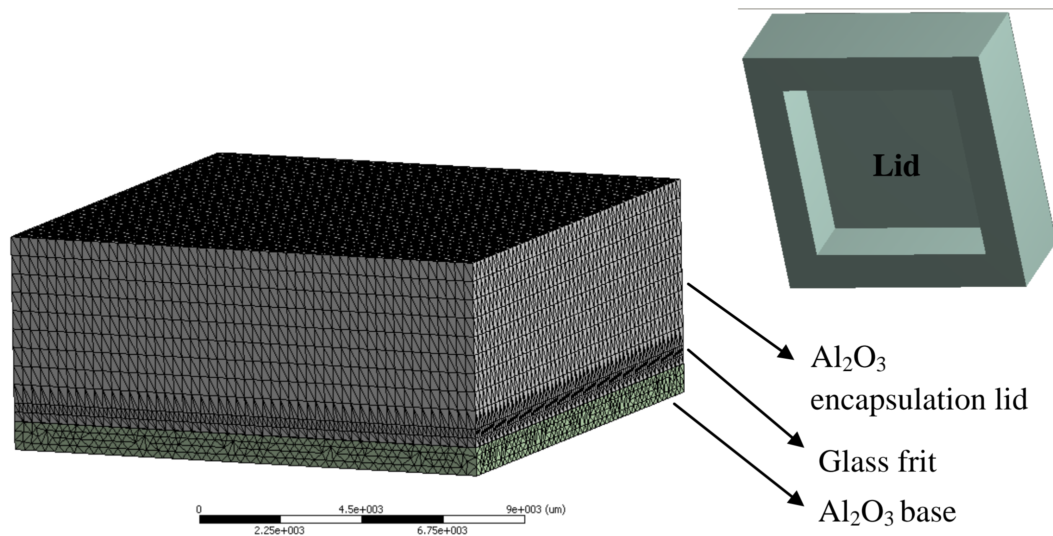

Figure 5.1: Lid attached to base package design

5.1.1 Effect of hydrostatic pressure on the package

In Figure 5.2, it shows the stress distribution of the Al_2O_3 encapsulation lid from the bottom up view. According to the Accuratus material data sheet [66] of Al_2O_3, the flexural strength is 379 MPa. The flexural strength for glass frit was calculated to be 152 MPa previously. Thus, these values were used as a reference level for simulation.

The simulation showed that when the package was subjected to 207 MPa of hydrostatic pressure, the centre region of the encapsulation lid experienced high stress concentration, represented by orange and red. The orange and red regions represent the point where the Al_2O_3 could possibly fail as the principle stress experienced in the region was above 379 MPa. This high stress was due to the presence of the cavity in the package, which in turn prevented the transfer or distribution of stress. Figure 5.3 shows the stress distribution of the Al_2O_3 base from the top down and bottom up view. From Figure 5.3 (a), it can be observed that the Al_2O_3 base area which the encapsulation lid sits on has a lower principle

stress as compared to the area that was exposed to the cavity. Similarly, this can be explained by the presence of a cavity which hindered the transfer of stress. In Figure 5.3 (b), minute orange and red zones formed at the outer corner edges of the base can be observed. Thus, it can be inferred that cracks may occur at the outer corner edges of the base when subjected to 207 MPa pressure. The significance of the failure due to cracks in the encapsulation lid outweighs that caused by cracks forming at the outer corner edge of the base. The failure of the encapsulation lid at the top may also result in the base to fail as there is no protection from the top to absorb the stress. In order to protect the base from failure, it was proposed by Phua, E. et al. [67] to increase the base thickness to above 3 mm as their experimental results proved that no failures were observed when the bases thickness is greater than 3 mm. Figure 5.4 shows the stress distribution of the glass frit from the top down view. Higher stress was observed on the outer corner edges of the glass frit layer. Even though the stress is higher on the outer corner edges, no cracks were formed as the principle stress at the region is much lower than 152 MPa. This could be because the glass frit is too thin to absorb the hydrostatic pressure. A study on the effect of different glass frit thicknesses will be discussed later.

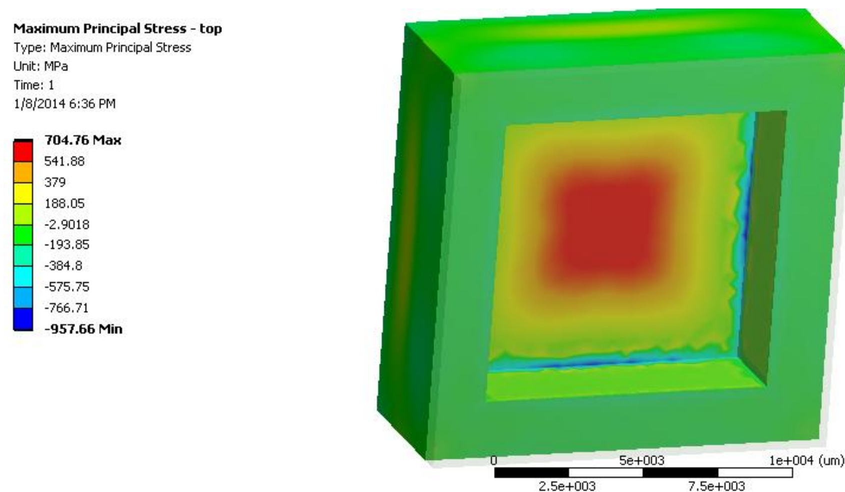

Figure 5.2: Stress distribution of the encapsulation lid subjected to 207MPa of hydrostatic pressure

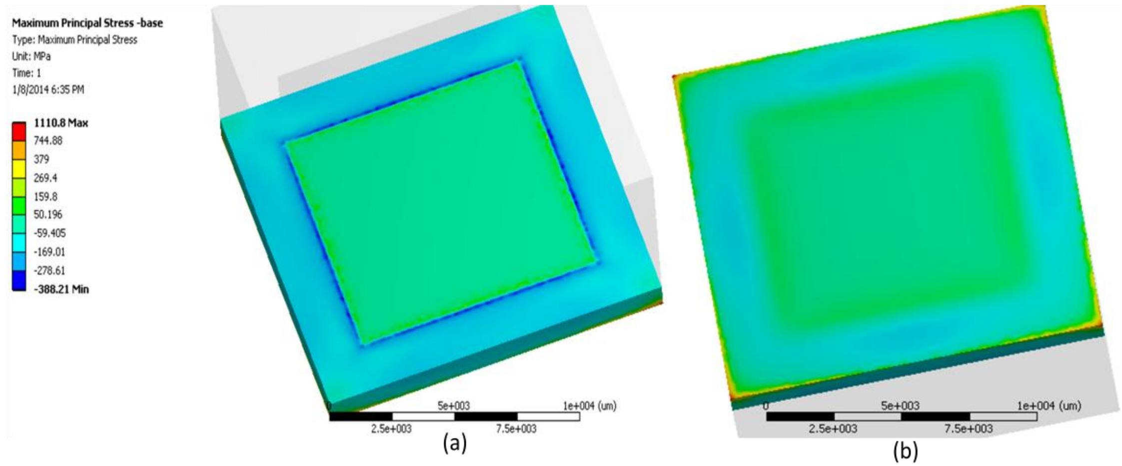

Figure 5.3: Stress distribution of the base subjected to 207MPa of hydrostatic pressure in: (a) Top down view (b) Bottom up view

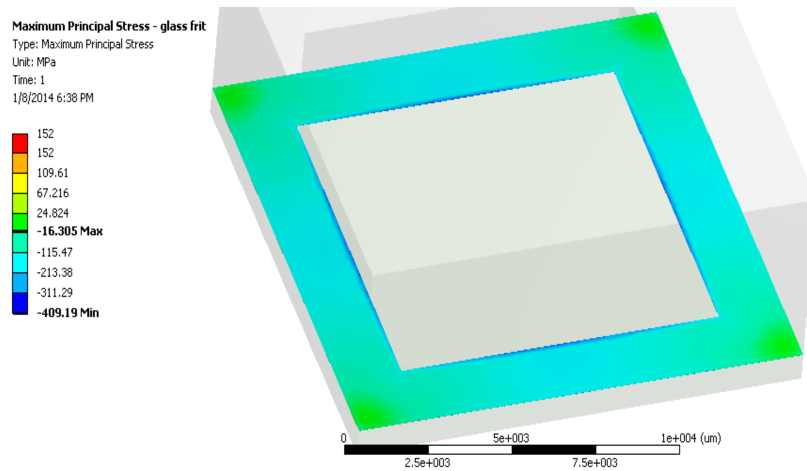

Figure 5.4: Stress distribution of the glass frit subjected to 207MPa of hydrostatic pressure

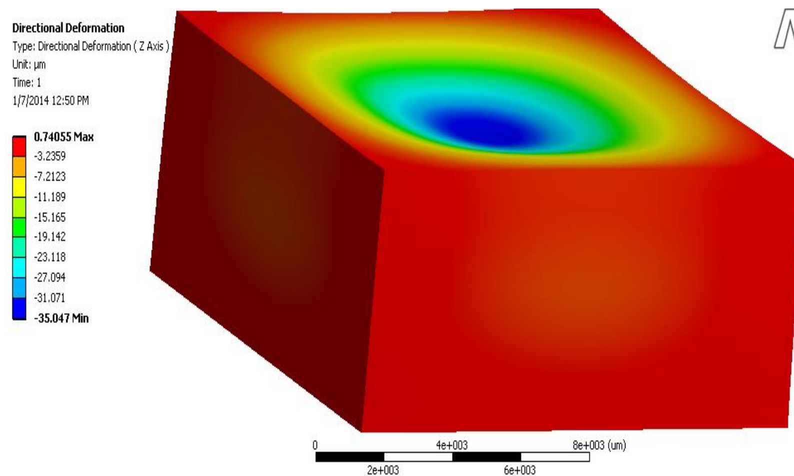

Figure 5.5: Directional deformation at z axis of the package subjected to 207MPa of hydrostatic pressure

Figure 5.5 shows the directional deformation along z axis of the package when it was subjected to a hydrostatic pressure of 207 MPa. It can be observed that the centre top lid experienced very high compressive stress and the rest of the region of the package experienced high tensile stress. The design of the encapsulation lid is unsuitable for experimental usage as the top centre region on the lid will most likely be damaged by the high pressure.

5.1.2 Effect of hydrostatic pressure on package with different glass frit thicknesses

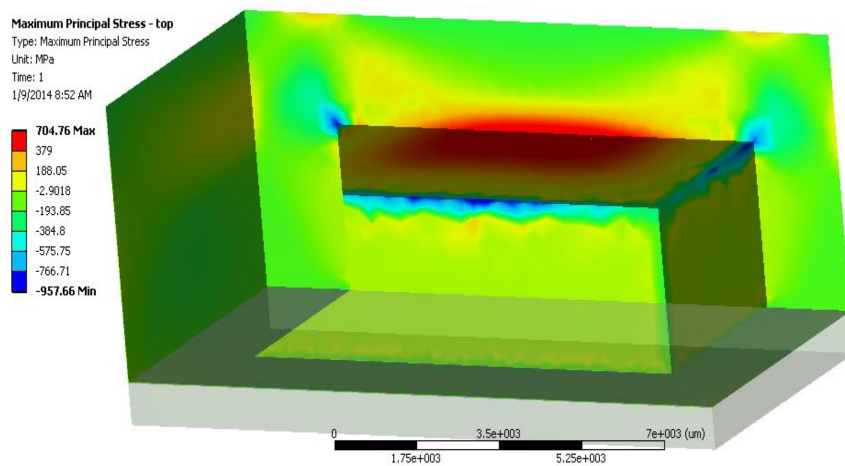

Figure 5.6: Stress distribution of the encapsulation lid with glass frit thickness of 0.00615 mm

The stress distribution in Figure 5.6 shows that the maximum principle stress concentration is located at the centre region of the encapsulation lid under 207 MPa of hydrostatic pressure. To determine the relationship between the maximum principle stress of the encapsulation lid and the change in glass frit thickness, the following plot was drawn after several simulations (see Figure 5.7).

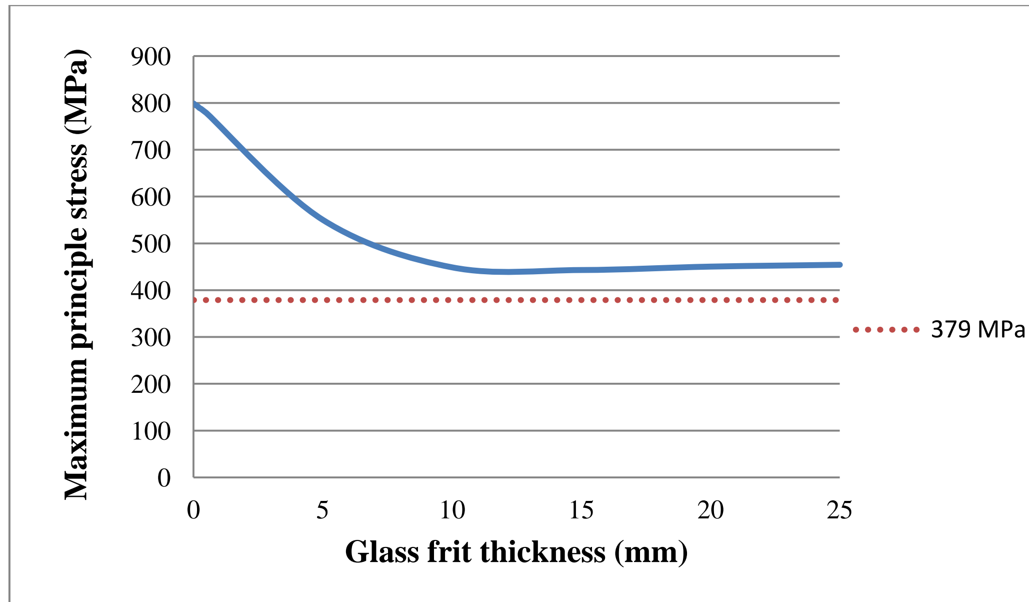

Figure 5.7: Maximum principle stress at the centre region of encapsulation lid versus the glass frit thickness

From Figure 5.7, it can be derived that as glass frit thickness increases, the maximum principle stress at the centre region of the encapsulation lid decreases and beyond 10 mm, the maximum principle stress starts to remain almost constant. This could be due to the transfer of stress onto the surface of the glass frit, thereby relieving the principle stress at the centre region of the encapsulation lid. This can be seen in Figure 5.8 where the maximum principle stress in glass frit thickness of 10 mm is above the flexural strength of the glass frit. Cracks would probably form on the bottom side of the glass frit when subjected to 207 MPa of hydrostatic pressure. Increasing the thickness of the glass frit would not reduce the maximum principle stress at the centre region of the encapsulation lid below the Al_2O_3 flexural strength of 379 MPa and beyond 10 mm, cracks would form on the glass frit. Furthermore, it is also experimentally impossible to increase the glass frit thickness to 10 mm.

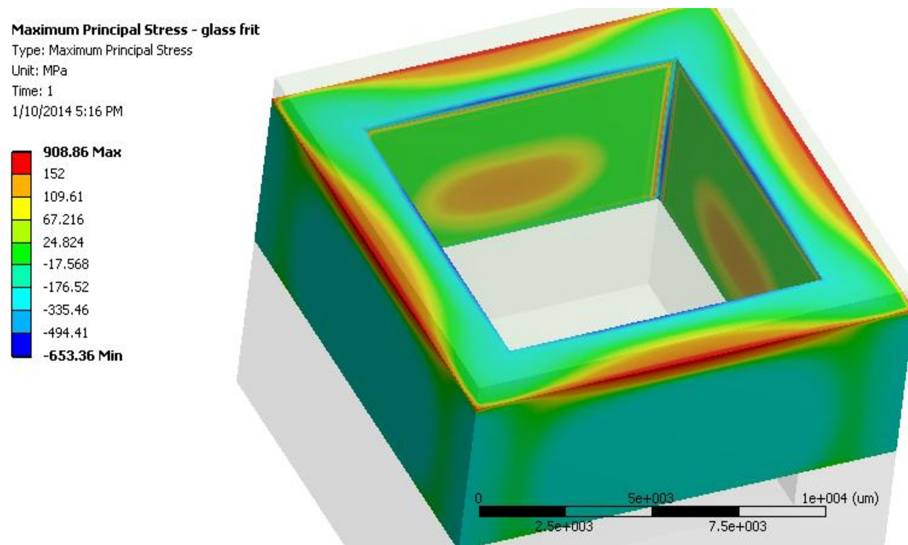

Figure 5.8: Stress distribution of the glass frit with thickness of 10 mm

Figure 5.9 shows the stress distribution of glass frit thicknesses of 0.00615 mm, 0.1 mm and 0.5 mm in a package subjected to 207MPa of hydrostatic pressure. It was observed that when the thickness of the glass frit increased from 0.00615 mm to 0.5 mm, the amount of principle stress on the inner surface of the glass frit layer also increased from -178.5 MPa to 79.688 MPa. This can be explained by the larger glass frit surface area at the outer surface exposed to hydrostatic pressure. With the cavity, no stress on the inner side of the glass frit can be transferred and resulted in high principle stress. Another possible reason could be that, as explained previously, when the thickness of the glass frit increases, the principle stress will be transferred from the centre region of the encapsulation lid onto the surface of the glass frit. Even though the principle stress on the glass frit increases with the glass frit thickness, the stress is still lower than the flexural strength of the glass frit, therefore no cracks or failure will occur.

Figure 5.9: Stress distribution of glass frit with thickness of:

(a) 0.00615 mm (b) 0.1 mm (c) 0.5 mm

From this, it can be concluded that the use of thicker glass frit can reduce a small amount of principle stress forming at the centre of the encapsulation lid but increases the principle stress on the glass frit layer. Therefore, a thicker encapsulation lid may be a possible solution to provide better stress resistance at the centre region of the encapsulation lid without inducing higher principle stress on the glass frit.

5.1.3 Effect of hydrostatic pressure on package with a thicker encapsulation lid

Figure 5.10 shows the stress distribution of a 6 mm thick Al_2O_3 encapsulation lid that was subjected to 207 MPa of hydrostatic pressure. The increase in the encapsulation lid thickness from 5 mm to 6 mm made it more stress-resistant as the maximum principle stress at the centre of the lid is 278.31 MPa, which is lower than the flexural strength of the Al_2O_3.

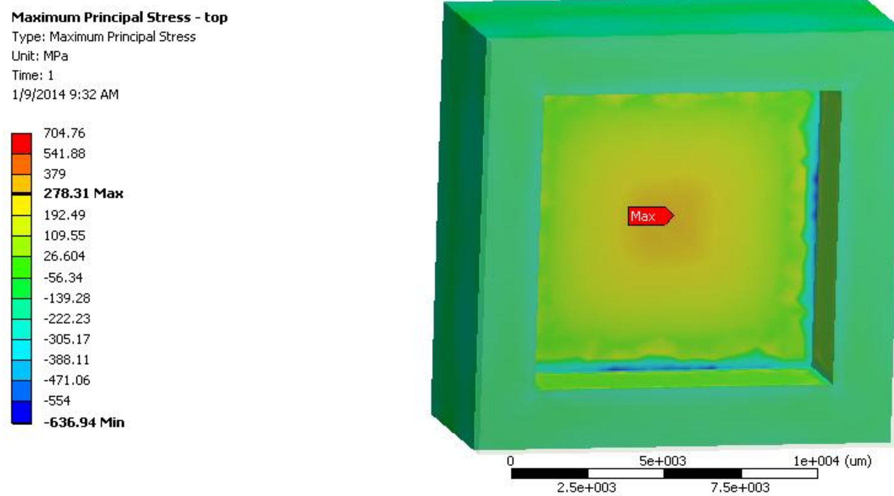

Figure 5.10: Stress distribution of 6 mm thick encapsulation lid subjected to 207MPa of hydrostatic pressure

The stress distribution in the base with the increase of Al_2O_3 encapsulation lid thickness (see Figure 5.11) shows that the maximum stress at the edge of the base in Figure 5.11 (b) became lower as compared to Figure 5.3 (b). Even though cracks may form at the outer

edge of the base, the cracks may not propagate through the bulk material as the bulk material experiences very low principle stress as compared to the corner edge.

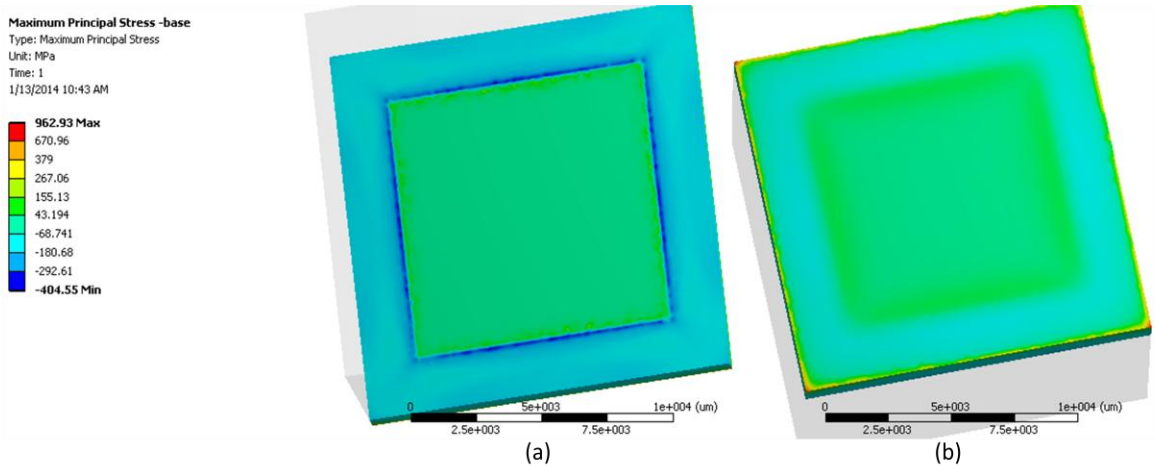

Figure 5.11: Stress distribution of base with 6 mm thick encapsulation lid subjected to 207MPa of hydrostatic pressure in: (a) Top down view (b) Bottom up view

As for the stress distribution in the glass frit with the increase of Al_2O_3 encapsulation lid thickness (see Figure 5.12), the maximum stress at the outer corner edge of the glass frit is much lower than the flexural strength of the glass frit. Therefore, increasing the thickness of the encapsulation lid further protects the glass frit and base from the high pressure by absorbing more pressure from the top.

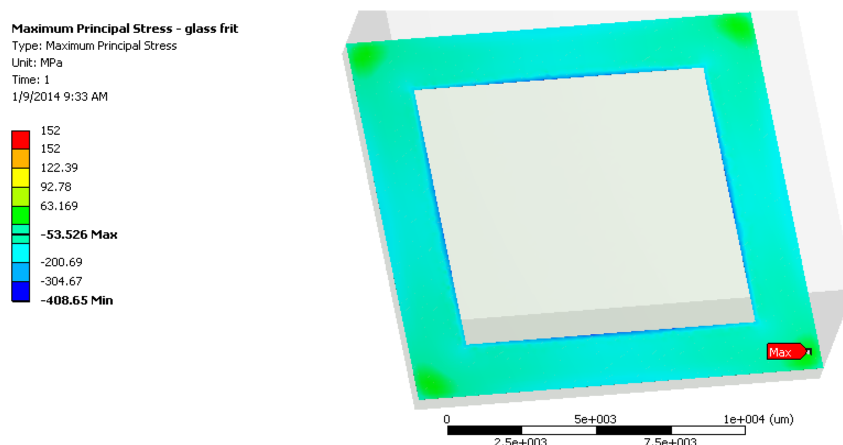

Figure 5.12: Stress distribution of glass frit with 6 mm thick encapsulation lid subjected to 207MPa of hydrostatic pressure

CHAPTER 6: CONCLUSION

This project aims to investigate the feasibility of using glass frit bonding in MCM hermetic encapsulation under harsh environments for industrial applications like deep sea oil rigs, industrial chemical or nuclear plants, geological surveys, space vehicles, and military installations. Glass frit bonding was chosen for the encapsulation of MCM due to its advantages discussed above.

From the initial characterisation of the AGC glass frit paste, it was determined to be of vitreous type bismuth-based glass frit and has a T_g of 366°C. The flexural strength of the glass frit was determined to be 152 MPa. SEM images of the glass frit bonding interface show that the Al_2O_3 can adhere well. Furthermore, the shear test results for Al_2O_3 to Al_2O_3 bonding using glass frit after aging for 500 hours at 300°C remains constant and above the MIL-STD 883G of 7.9 MPa. This implies that the bond between the Al_2O_3 and glass frit remains strong despite thermal aging. Glass frit bonding was used for encapsulation on Al_2O_3 packages and all the samples, except one, passed the MIL-STD 883G after thermal aging for 500 hours at 300°C. Therefore, it proves that using glass frit bonding for Al_2O_3 MCM hermetic encapsulation under high temperature environment is feasible.

ANSYS^{TM} simulation has shown that glass frit is able to withstand high pressure testing of 207 MPa without forming possible cracks. While an increase in glass frit thickness resulted in a slight decrease in principle stress on the encapsulation lid, it increases the principle stress on the inner surface of the glass frit. When the thickness of the encapsulation lid was increased to 6 mm, not only did the lid became more stress-resistant

and was able to tolerate 207 MPa of hydrostatic pressure, the principle stress on the glass frit and base became lower.

To conclude, glass frit bonding is an excellent hermetic encapsulation sealant against high temperature environment of 300°C and is also suitable for high-pressure environment of 207 MPa according to both experiments and simulation respectively.

CHAPTER 7: FUTURE WORK

The future work of this project will be discussed as follows:

1. To characterise the voids present at the package sealed area by using Computed Tomography (CT) scan as the equipment is able to determine the level of the glass frit bonding in which voids are present and scan for any fine cracks.

2. Ceramic to ceramic samples, bonded using glass frit bonding, will be thermal aged at a higher temperature of 350°C, 400°C and 450°C for 500 hours and sheared to find out the shear strength of the glass frit bonding on ceramic and also to investigate the possible failure mechanism under even higher temperatures.

3. According to Chidambaram, V. et al. [1], ruggedized electronics used for deep sea oil rig data acquisition have to withstand a high pressure of 207 MPa. This amount of pressure is equivalent to two full-grown, male African elephants acting on the electronic devices. Therefore, it is very important to ensure that the hermetic seal of the ceramic package using glass frit bonding does not fail during the 500 hours of high pressure. CIP will be used to apply pressure on the sealed packages and check for the survivability of the package by measuring the helium leak rate of the ceramic package. The sealed package can then be placed in a high temperature and high pressure tester and check for the helium leak rate.

4. Wiemer, M. et al. [68] has reported that there is no influence from the glass frit bond to the aluminium signal lines when the lines are embedded in the paste for MEMS devices. Likewise, to ensure that copper metallisation (signal lines) can also run through the sealing layer without affecting the hermeticity of the ceramic

package, helium leak test on package with signal lines as well as electrical testing on the effects of the bonded glass frit on the signal lines, will be considered. Apart from hermeticity and electrical testing, mechanical testing of the glass frit bonding between the metal and ceramic by measuring the bonding strength of it can be done (see Figure 7.1).

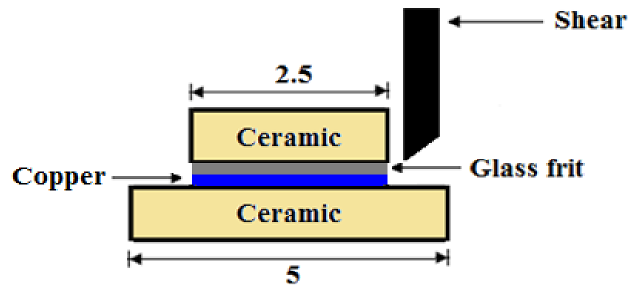

Figure 7.1: Shear test for ceramic-copper-glass frit-ceramic sample

5. According to the formulae shown below, R, which is the throughput per sec for helium leak test is directly proportional to the square root of temperature. Although the temperature effect is minor due to the square root, it has to be taken account of when temperature increases. Therefore, will need an in situ helium leak detector with a heater to correctly measure the leak rate under higher temperature.

$$R = F\sqrt{\frac{T}{M}}(P_1 - P_2)$$

P_1 = Partial pressure on the high side

P_2 = Partial pressure on the low side

F = Molecular conductance of the leak channel

R = Throughput per second

T = Temperature in degrees K

M = Molecular weight of the leaking gas

REFERENCES

1. V. Chidambaram, B.Y. Ho & S.Gao, "Reliability of Au-Ge and Au-Si Eutectic Solder Alloys for High-Temperature Electronics," *J. Electron. Materials*, vol. 41, no. 8, pp. 2107–2117, Apr. 2012.

2. K. Notzold, J. Graf & R.Muller-fiedler, "A four-point-bending-test for the stability assessment of glass frit bonded molded microsensors,"*Microelectronics Reliability*, vol. 48, pp. 1562–1566, 2008.

3. J.S. Chang, J.Y. Lin & S.C. Ho, "Wafer level glass frit bonding for MEMS hermetic packaging,",

4. T. Kujawa & W. Nowak, "Winning the geothermal heat energy in one hole and two-hole systems," *Int. Geothermal Conf.*, pp. 1–9, Sep. 2009.

5. J.S. Harder & D.A. Meyer, "Hermetic Packaging for Power Multichip Modules,",

6. R. Knechtel, "Glass frit bonding: An universal technology for wafer level encapsulation and packaging," vol. 12, pp. 63–68, 2005.

7. S. Patel, D. Delaney & D.X. Xu, "Characterization of Glass on Electronics in MEMS," *Spie Conf. Materials Device Characterization Micromachining*, vol. 3875, pp. 73–78, 1999.

8. W.H. Ko, "Packaging of microfabricated devices and systems," *Materials Chemical and Physics*, vol. 42, pp. 169–175, 1995.

9. S. Farrens & S. Sood, "Wafer Level Packaging: Balancing Device Requirements and Materials Properties,",

10. R. Zhang, R.W. Johnson & D.Shaddock, "Characterization of Thick Film Technology for 300°C Packaging," *2010 High Temperature Electron. Conf.*, May. 2010.

11. T. Zhang & D. Shaddock, "Characterization of LTCC-Thick Film Technology for 300°C Packaging," *2011 Hiten*, Jul. 2011.

12. M. H. Cohen, D. Turnbull, J. Chem. Phys., 1959, 31, 1164.

13. K.A. Jackson, "Diffusion in Amorphous Materials," in *Kinetic Processes: Crystal Growth, Diffusion, and Phase Transitions in Materials*, 2nd ed., Germany: Wiley-Vch, pp. 19–26, 2010.

14. S.H. Choa, "Reliability study of hermetic wafer level MEMS packaging with through-wafer interconnect," *Microsystem Technology*, vol. 15, pp. 677–686, 2009.

15. A. Pregelj, "Leak detection methods and defining the sides of leaks," *The 4th Int. Conf. Solvenian Society for Nondestructive Testing*, 1997.

16. Q. Wu, N. Lorenz & K.Cannon, "Hermetic joining of micro-devices using a glass frit intermediate layer and a scanning laser beam," *2nd Electron. Systemintegration Technology Conf.*, pp. 669–678, 2008.

17. F.J. Norton, "Helium diffusion through glass," *American Ceramic Society*, 1952.

18. P. Weiss, "MEMS & MOEMS reliability: wafer-level packaging and low-temperature processing issues," *Proc. 2005 IEEE/lEOS Workshop Fibres Optical Passive Components*, pp. 75–86, 2005.

19. H.D. Chang, C.A. Huang & S.Liu, "High hermetic performance of glass frit for MEMS package,",

20. R. Knechtel, "Wafer bonding technologies in industrial MEMS processing," *ECS Transcations*, vol. 3, no. 6, pp. 341–354, 2006.

21. B. Muller & A. Stoffel, "Tensile strength characterization of low-temperature fusion bonded silicon wafers," *J. Micromechanical Microengineering*, vol. 1, pp. 161–166, Jun, 1991.

22. J. Wei, H.N. Xie & C.K. Wong, "Low temperature wafer anodic bonding," *J. Micromechanics Microengineering*, vol. 13, p. 217–222, 2003.

23. A. Manneborg, M. Nese & P.Bhlckers, "Silicon-to-silicon anodic bonding with a borosilicate glass layer," *J. Micromechanical Microengineering*, vol. 1, pp. 139–144, 1991.

24. P. Mrozek, "Anodic bonding of glasses with interlayers for fully transparent device applications," *Sensors and Actuators A: Physical*, vol. 151, pp. 77–80, 2009.

25. H. Henmi, S. Shoji & Y.Shoji, "Vacuum packaging for microsensors by glass-silicon anodic bonding," *Sensors and Actuators a*, vol. 43, pp. 243–248, 1994.

26. M. Esashi, "Topical Review: Wafer level packaging of MEMS," *J. Micromechanics Microengineering*, vol. 18, pp. 1–13, 2008.

27. W.T. Park, J.W. Jang & T.Clare, "Microstructure and mechanical properties of aluminium-germanium eutectic bonding with polysilicon metallization for microelectromechanical systems (MEMS) packaging," *Scripta Materialia*, vol. 64, pp. 733–736, 2011.

28. B.G. Jeong, S.J. Ham & C.Y. Moon, "Reliability verification of hermetic package with nanoliter cavity for RF-Micro device," *IEEE Trans. Advanced Packaging*, vol. 33, no. 1, pp. 64–71, Feb, 2010.

29. S. Farrens, "Wafer-Bonding Technologies and Strategies for 3D ICs," *SUSS Microtec*, pp. 1–35, 2008.

30. C.S. Tan, J. Fan & D.F. Lim, "Low temperature wafer-level bonding for hermetic packaging of 3D microsystems," *J. Micromechanical Microengineering*, vol. 21, pp. 1–6, 2011.

31. B. Swinnen, W. Ruythooren & P.De Moor, "3D integration by Cu-Cu thermo-compression bonding of extremely thinned bulk-Si die containing 10 µm pitch through-Si vias," *IMEC*.

32. P.K. Khanna, S.K. Bhatnagar & W.Gust, "Analysis of Packaging and Sealing Techniques for Microelectronic Modules and Recent Advances,"*Microelectronics Int.*, pp. 8–12, 1999.

33. Y. Jin, Z.F. Wang & P.C. Lim, "MEMS Vacuum Packaging Technology and Applications," *2003 Electron. Packaging Technology Conf.*, pp. 301–306, 2003.

34. A.P. Malshe, C. O'neal & S.B. Singh, "Challenges in the Packaging of MEMS,"*Int. Microelectronics Packaging Society*, vol. 22, no. 3, pp. 233–241, 1999.

35. M. Ebert & J. Bagdahn, "Determination of residual stress in glass frit bonded MEMS by Finite Element Analysis," *5th Int. Conf. Thermal Mechanical Simulation Experiments Micro-Electron. Micro-Syst.*, pp. 407–412, 2004.

36. M. Petzold, C. Dresbach & M.Ebert, "Fracture Mechanical life-time investigation of glass frit-bonded MEMS sensors," *IEEE*, pp. 1343–1348, 2006.

37. R. Knechtel, "Characterization and Qualification of Wafer-bonded MEMS device," *The Electrochemical Society*, vol. 16, no. 8, pp. 417–424, 2008.

38. Z. Sun, D. Pan & J.Wei, "Ceramics Bonding Using Solder Glass Frit," *J. Electron. Materials*, vol. 33, no. 12, pp. 1516–1523, 2004.

39. R. Knechtel, M. Wiemer & J.Fromel, "Wafer level encapsulation of microsystems using glass frit bonding," *Microsyst Technol*, vol. 12, pp. 468–472, 2006.

40. Lorenz, M. Desmulliez & D.P. Hand, "Hermetic glass frit packaging in air and vacuum with localised laser joining," *J. Micromechanics Microengineering*, vol. 21, pp. 1–7, 2011.

41. J. Martin, "Wafer capping of MEMS with Fab-friendly metals," *Proc. SPIE*, vol. 6463, pp. 1–6, 2011.

42. B. Boettge, C. Dresbach & A.Graff, "Mechanical characterization and micro structure diagnostics of glass frit bonded interfaces," *Ecs Trans.*, vol. 16, no. 8, pp. 441–448, 2008.

43. Sadoway, D. R. (2009). *Lecture 21: Engineered Glasses: Network Formers, Network Modifiers, Intermediates – Properties of Silicate Glasses - Metallic Glass*. Retrieved January 26, 2012 from Massachusetts Institute of Technology, MIT, Web site: http://videolectures.net/mit3091f04_sadoway_lec21/

44. K. Notzold, C. Dresbach & J.Graf, "Temperature dependent fracture toughness of glass frit bonding layers," *Microsystem Technology*, vol. 16, pp. 1243–1249, 2010.

45. Tarr, M. (2011). *Screen and stencil printing*. Retrieved March 14, 2012 from http://www.ami.ac.uk/courses/topics/0222_print/

46. C.Y. Chen, C.H. Hung & J.Y. Jhong, "Demonstration of wafer capping through glass frit bonding and its application on molded platform package,",

47. X. Chen, P.L. Yan & J.J. Tang, "Application of WLP with Barrier Trench Structure in Precision Screen Printing Technology by Glass Frit," *2010 11th Int. Conf. Electron. Packaging Technology & High Density Packaging*, pp. 71–73, 2010.

48. W.C. Oliver & G.M. Pharr, "Journal of Materials Research," *An Improved Technique for Determining Hardness and Elastic Modulus Using Load and Displacement Sensing Indentation Experiments*, vol. 7, no. 6, pp. 1564–1583, Jun. 1922.

49. C. Anthony, *Nanoindentation.* 3rd ed., New York: Springer New York Dordrecht Heidelberg London, 2011, p. 34.

50. (2012), *Poisson's ratio*. Available from: http://www.engineeringtoolbox.com/poissons-ratio-d_1224.html [Accessed: September 15, 2013].

51. J.M. Gere, *Mechanics of Materials.* 6th ed., United States of America: Thomson Learning, p. 400, 2004.

52. (2012), *Modulus of Elasticity - Young Modulus for some common Materials*. Available from: http://www.engineeringtoolbox.com/young-modulus-d_417.html [Accessed: September 13, 2013].

53. C. Suryanarayana & M.G. Norton, "Lattices and Crystal Structures," in *X-Ray Diffraction: A Practical Approach*,, New York: Plenum Publishing Corporation, p. 61, 1998.

54. W.D. Brown, *Advanced Electronic Packaging with emphasis on multichip module.*, United states of America: IEEE press, p. 22, 1999.

55. S.B. Shim, D.S. Kim & S.J. Hwang, "Wetting and surface tension of bismate glass melt," *Thermochimica Acta*, vol. 496, pp. 93–96, 2009.

56. I. Dyamant, D. Itzhak & J.Hormadaly, "Thermal properties and glass formation in the SiO2-B2O3-Bi2O3-ZnO quaternary system," *J. Non-crystalline Solids*, vol. 351, pp. 3503–3507, 2005.

57. B.S. Kim, E.S. Lim & J.H. Lee, "Thermal and electrical properties of Bi2O3-B2O3-ZnO glasses for the application to plasma display panel," *Department Inorganic Materials Eng.*.

58. R. I Made, S.S. Pramana & E.Phua, "Study of Metal Additives to Alumina Substrate for High Temperature and Pressure Application," *IEEE 14th Electron. Packaging Technology Conf.*, pp. 48–51, 2012.

59. W. Pompe, G. Rodel & H.J. Weiss, *Bio-Nanomaterials: Designing Materials Inspired by Nature.*, 2013,

60. J.E. Shelby, *Introduction to glass science and technology.* 2nd ed., United Kingdom: TJ International Ltd, Padstow, Cornwall, p. 192, 2005.

61. Griffith A.A. 1921 Phil. Trans. Roy. Soc. London A221 163–198

62. E.E. Gdoutos, *Fracture mechanics: An introduction.* 2nd ed., Netherlands: Springer, pp. 5–13, 2005.

63. M. Ciccotti, "Stress-corrosion mechanisms in silicate glasses," *J. Physics D: Applied Physics*, vol. 2, pp. 1–30, Apr. 2009.

64. R.R. Acher & T.J. Lardner, *An introduction to the mechanics of solids.* 2nd ed., US: McGraw-Hill, 1999,

65. S.M. Wiederhorn & L.H. Bolz, "Stress Corrosion and Static Fatigue of Glass,"*J. American Ceramic Society*, vol. 53, no. 10, pp. 543–547, Oct. 1970.

66. Aluminum Oxide, Al2O3 Ceramic Properties (2013). Retrieved November 5, 2013 from Accuratus Ceramic Corporation, Web site: http://accuratus.com/alumox.html

67. E. Phua, R. I Made & A.Sharif, "Electronic packages for high pressure applications: A dome-shaped cavity design," *2013 Electron. Components & Technology Conf.*, pp. 2342–2348, 2013.

68. M. Wiemer, J. Fromel & C.Jia, "Bonding and contacting of MEMS-structures on Wafer level," *Fraunhofer Institute of Reliability and Microintegration*.

APPENDIX 1

Indentation	Young’s Modulus
1	62.778
2	62.269
3	61.714
4	66.678
5	61.924
6	56.399
7	64.880
8	55.050
9	61.087
10	61.720
11	61.181
12	62.740
13	61.663
14	58.826
15	64.418
16	57.973
17	57.427
18	56.889
19	58.015
20	61.604
21	56.800
22	58.811
23	58.190
24	57.470
25	56.407
26	55.396
27	56.740
28	57.154

29	55.107
30	58.078
31	62.064
32	54.106
33	55.650
34	56.120
35	56.124
36	59.322
37	54.299
38	61.537
39	58.591
40	55.596
Average	**58.970**
Standard Deviation	**3.175**